Supporting Information

Effects of Catalyst Phase on the Hydrogen Evolution Reaction of Water Splitting: Preparation of Phase-Pure Films of FeP, Fe_2P, and Fe_3P and their Relative Catalytic Activities

Desmond E. Schipper,[†,1] Zhenhuan Zhao,[ϕ, Δ,1] Hari Thirumalai,[ψ] Andrew P. Leitner,[†] Samantha L. Donaldson,[†] Arvind Kumar,[†] Fan Qin,[ϕ,Δ] Zhiming Wang,[Δ] Lars C. Grabow,[ψ*] Jiming Bao,[ϕ,Δ*] and Kenton H. Whitmire[†*]

[†]Department of Chemistry, Rice University, Houston, TX 77005, United States

[ϕ]Department of Electrical and Computer Engineering and [ψ]Department of Chemical and Biomolecular Engineering, University of Houston, Houston, Texas 77204, United States

[Δ]Institute of Fundamental and Frontier Sciences, University of Electronic Science and Technology of China, Chengdu 610054, China

[1]These authors contributed equally.

*whitmir@rice.edu (K.H. Whitmire), *jbao@uh.edu (J. Bao) *grabow@uh.edu (L. C. Grabow)

Table of Contents: **Page(s)**

1. Film Deposition:

Film deposition was carried out in a similar manner as previously reported.[6] Key differences are that the distances of the tip of the metal stage to the end of the tube and the start of the heating zone were varied according to **x** and **y** in **Figure S1**. Another key difference is that small boats/cups made out of aluminum foil (1 cm deep, 1 cm in diameter) were used to weigh and transfer the precursor to the bottom of the tube, which made it easier to get the precursor to the bottom of the tube without having any to stick to the walls. This was especially helpful when working with **2** as it is a liquid. Substrates were cut into ~20.5mm x 11 mm sections and affixed to the stage with silver paste. The material production parameters are given in **Table S1**. After deposition, the heating zone was shifted forward to envelop the stage and the material on the substrate allowed to anneal for two hours at the deposition temperature before slow cooling to room temperature. Note: Fe_3P was annealed for 24 h at 550 ^oC to get a satisfactorily crystalline material, which was then used for HER testing. The unannealed PXRD for the Fe_3P on FTO is given in **Figure S25**. An aluminum foil jacket was placed over the end of the tube for Fe_3P deposition to encourage volatilization of the precursor.

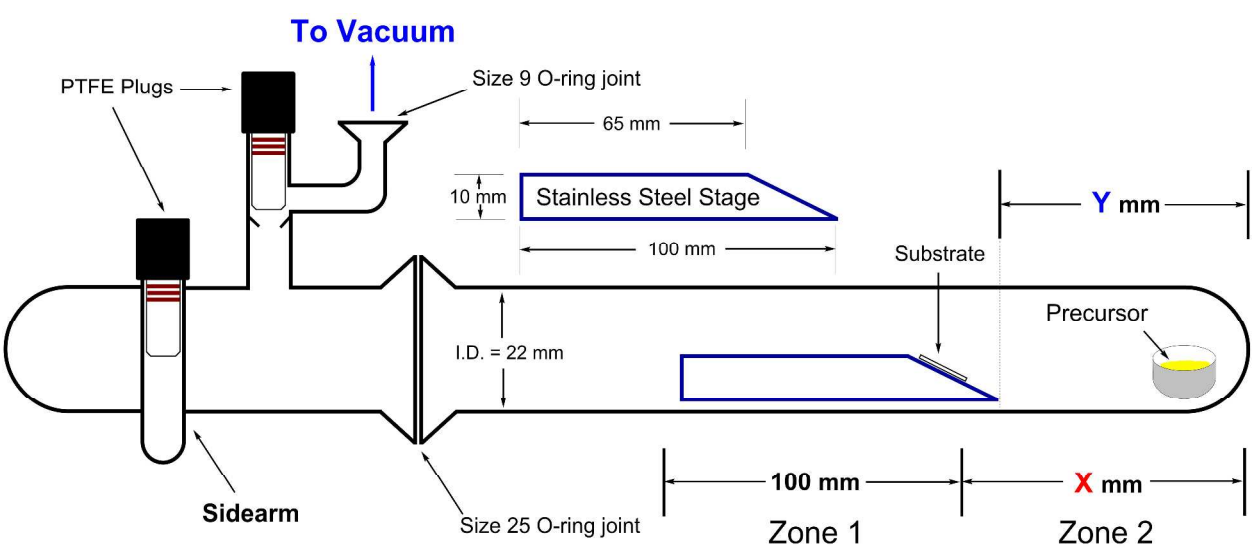

Figure S1. The deposition apparatus. **X** and **Y** parameters for each deposition can be found in **Table S1**.

Table S1: Film Deposition Parameters							
Material Produced	**Precursor**	**Precursor Amount (mg)**	**Decomp. Temp. (Zone 1, ^{o}C)**	**Decomp. Time Allowed**	**X (mm)**	**Y (mm)**	**Substrate(s)**
FeP	**2**	25 (2-3 drops)	450	15 m.	75	55	FTO/Quartz
FeP	**3**	25 mg	350	8 h	75	55	Quartz
Fe_2P	**1**	20 mg	350	15 m	75	45	FTO/Quartz
Fe_3P	**4**	25 mg	400	3 h	75	55	FTO
FeP/Fe_2P Mixture	**1**	25 mg	450	15 m	75	45	Quartz

2. Detection of Phosphine from the CVD Decomposition of 1:

300 mg of **1** was loaded into the end of the apparatus tube and the apparatus placed under high vacuum as with a typical deposition, although without the stage, and zone **2** was kept cold with liquid nitrogen. The heating zone was raised to 350 ^{o}C, and the sidearm (see **Figure S1**) was immersed in liquid nitrogen, zone **2** allowed to warm to room temperature, and the valve to dynamic vacuum closed. After 20 minutes, dynamic vacuum was re-applied and zone **1** allowed to cool to room temperature. The sidearm was closed and kept at liquid nitrogen temperatures as the apparatus was closed and transferred to a Schlenk line. To the still-frozen sidearm was added approximately 3 mL d^8-toluene via cannula, and the temperature was allowed to rise to approximately room temperature. The solution was then transferred via cannula to a septum capped NMR tube which had been flushed with nitrogen and the NMR experiments were carried out within an hour. The spectra show the presence of phosphine given the quartet at -242.78 ppm ($J_{P\text{-}H}$ = 186 Hz) in the ^{31}P spectrum and the doublet at 1.592 ppm ($J_{P\text{-}H}$ = 186 Hz). No other P signals could be detected.

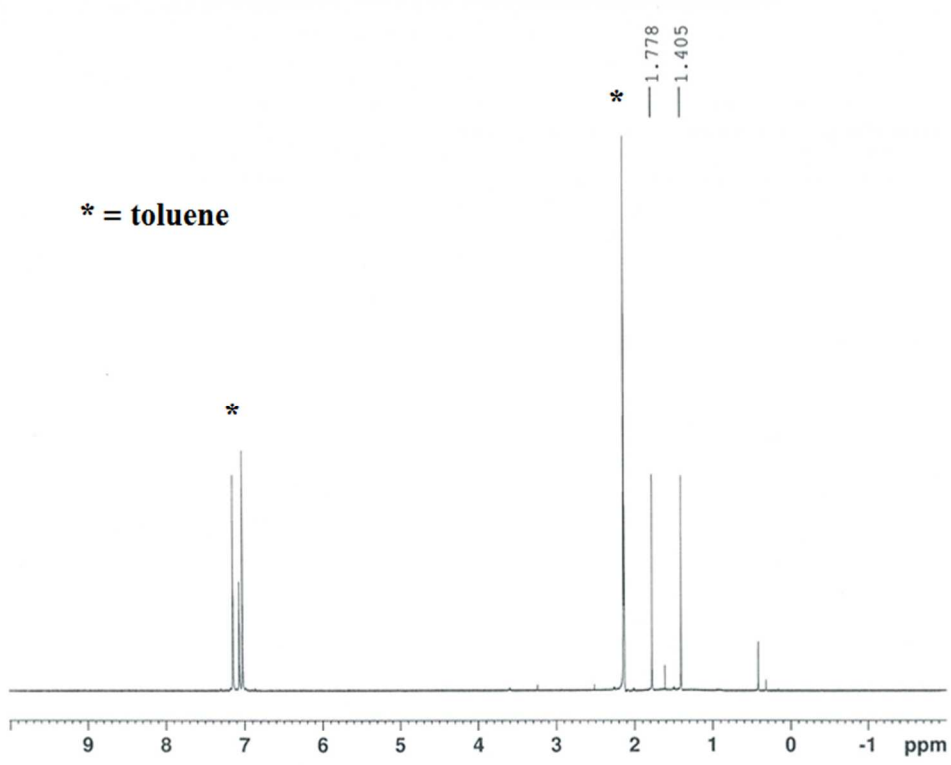

Figure S2. ^{1}H NMR Spectrum of the Off-Gases of the CVD using compound **1**

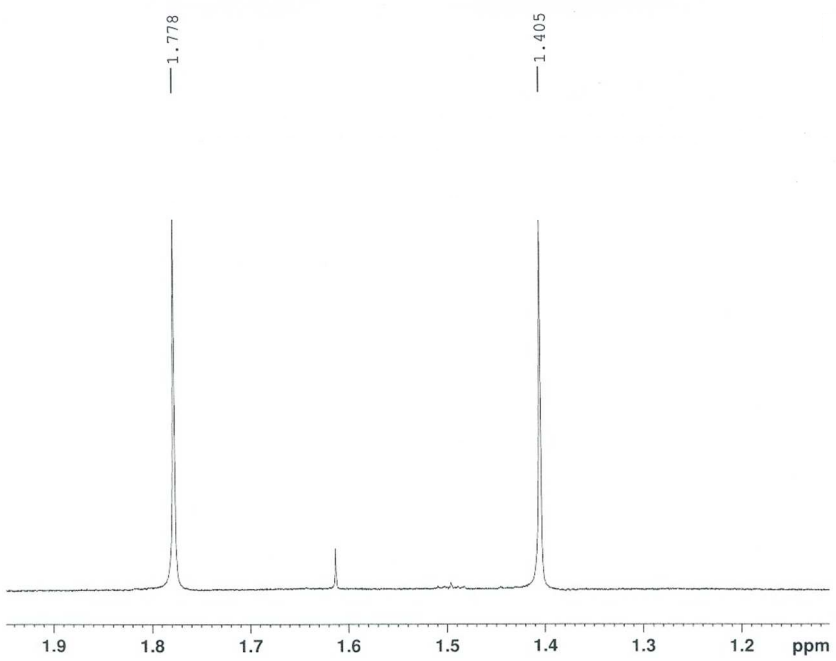

Figure S3. ^{1}H NMR Spectrum in the P-H window from CVD using compound **1**

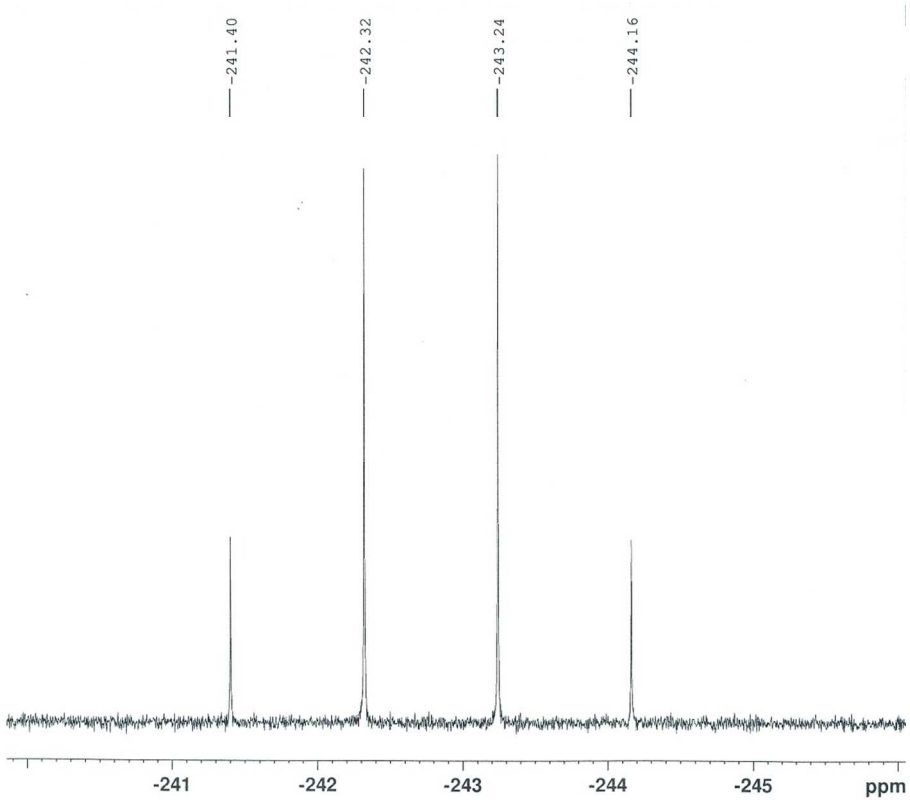

Figure S4. ^{31}P NMR Spectrum of the Off-Gases of Compound **1** CVD Decomposition

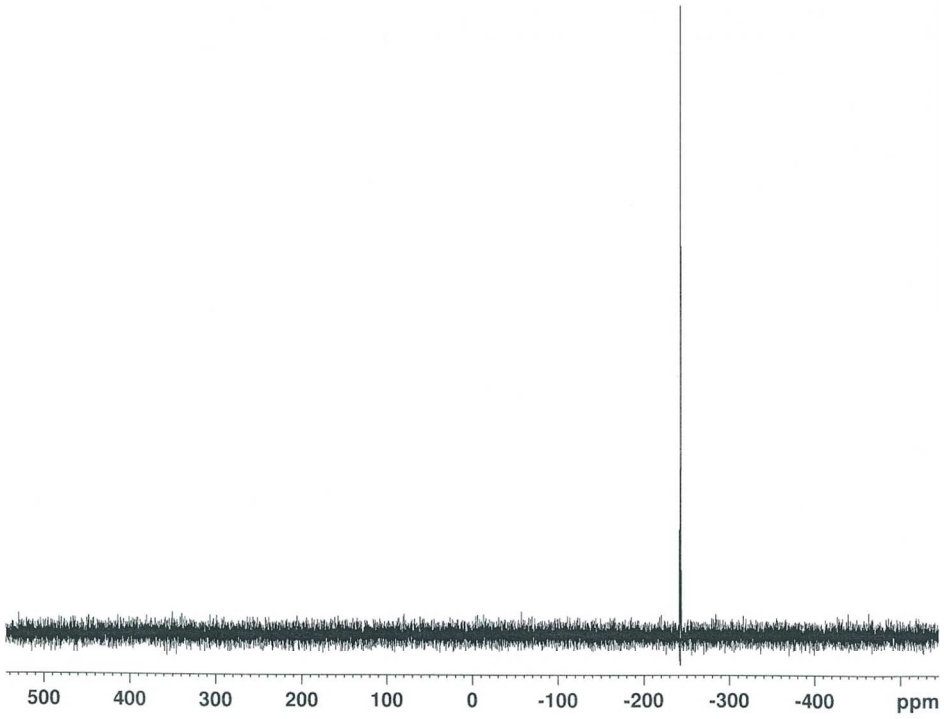

Figure S5. ^{31}P NMR Spectrum of the Off-Gases of Compound **1** CVD Decomposition. Full window.

3. General Considerations and Experimental Details

The precursors $Fe(CO)_4PH_3$ (**1**),[1] $Fe(CO)_4P^tBuH_2$ (**2**),[2] and $H_2Fe_3(CO)_9P^tBu$ (**4**)[3] were prepared according to literature methods and standard Schlenk technique. **3** is a new compound and its synthesis is reported below. Sodium hydroxide, *tert*-butyldichlorophosphine as a 1.0 M solution in diethyl ether, methanol, and iron pentacarbonyl were obtained from Sigma Aldrich and used without further purification before use. Sodium hydride as a 60% dispersion in mineral oil was rinsed with hexane (10 mL per 1 g NaH dispersion, three times) prior to use. Synthetic manipulations were performed exclusively under a dry nitrogen atmosphere, and solvents as well as iron pentacarbonyl were degassed prior to use.

Compounds **1**, **2**, and **3** were stored at -10 ^oC under nitrogen while **4** was stored at room temperature in a nitrogen-filled glovebox. FTO glass (TEC 7, with resistivity of 6−8 $\Omega\cdot cm^{-2}$) was obtained from Hartford Glass Co. and cut into ~1 cm x 2 cm pieces. Quartz microscope slides (1 mm thick) were obtained from Ted Pella Inc. Films were stored under ambient conditions after deposition. XPS measurements and depth profiling were performed using a Physical Electronics PHI Quantera SXM instrument with a monochromatic aluminum Kα source operated at 40.7 W with a beam size of 200μm and a take-off angle of 45º. The spectra were referenced to surface adventitious carbon (284.8 eV). The films were depth-profiled with a 2 mm × 2 mm 4 keV Ar^+ beam with 0.5 mA current. An FEI Quanta 400 instrument was used to obtain SEM images. Powder-XRD scans were collected on a Rigaku Ultima II vertical θ-θ powder diffractometer using Cu Kα radiation with Bragg-Brentano para-focusing optics. ^1H and ^{31}P NMR data were recorded on a 500 MHz Bruker spectrometer (202 MHz for ^{31}P). ESI-MS data were collected on a Bruker Daltonics microTOF ESI/MS coupled with an Agilent 1200 HPLC instrument. Elemental analyses were performed by Galbraith Laboratories Inc.

Synthesis of 3: To a chilled (-10 ^oC) suspension of sodium hydroxide (1.9 g, 46 mmol) in 10 mL of methanol was added 2 mL of iron pentacarbonyl (15 mmol) and the resulting solution stirred at 1 h at this temperature before warming to RT after which the solution was allowed to stir for 20 h. The solvent was then removed *in vacuo* and the solids thoroughly dried. To the resulting solids were then added 80 mL of tetrahydrofuran to extract $Na[HFe(CO)_4]$, the solution of which was filtered into a flask containing 0.1865 NaH (7.8 mmol). Strong bubbling signaling the release of hydrogen concomitant with the formation of $[Fe(CO)_4]^{2-}$ was observed which subsided after 30 m at which point an infrared spectrum of the

solution indicated the presence of both $[Fe(CO)_4]^{2-}$ and $[HFe(CO)_4]^-$. Then, 14 mL of a 1 M solution of P^tBuCl_2 (14.0 mmol) in diethyl ether was added in 2 mL aliquots spread over five minutes accompanied by a change in color from brown-orange to yellow-orange. After stirring overnight, the solvent was removed *in vacuo* and the solid treated with hexane (80 mL) and filtered. The filtered solution was then reduced to an oil *in vacuo* and left to crystallize at -10 ^oC. After three days at this temperature, large masses of crystals were found in the oil which was filtered off. The crystals were washed with 10 mL of hexane to yield 0.41 g (9.4% yield) of crystalline **3**. The filtered oil continued to produce crystals of **3** upon standing at room temperature and after two weeks of standing yielded another 0.47 g of product for a total yield of 23.6%. Elemental analysis calc: C: 37.54%, H: 3.54%, N: 0%. Found: C: 36.79%, H: 3.44%, N: <0.50%. ν_{CO} (hexanes): 2067.78(m), 2054.63(s), 2017.63(m), 1987.78(s), 1979.28(vs), 1974.15(vs), 1963.15(vs), 1945.20(vw) cm^{-1}. M.pt. 117-125 ^oC. ESI-MS Data for crystalline **3**: *m*/*z* (%) 512.9 (76) [**3**-H^+]$^-$, 484.9 (32) [**3**-H^+- CO]$^-$, 456.9 (66) [**3**-H^+-2 CO]$^-$, 428.9 (33)[**3**-H^+- 3 CO]$^-$, 400.9 (100)[**3**-H^+- 4 CO]$^-$, 372.9 (14) [**3**-H^+- 5 CO]$^-$. ^{1}H-NMR data (C_6D_6, ppm): **3** exhibits a complex second-order spectrum consistent with the two components which could arise from hindered rotation about the P-P bond. The first P-H multiplet is centered at 4.81; the second P-H multiplet is centered at 4.73 ppm. The *t*-butyl regions overlap with the envelope centered at 0.92 ppm. The P-H and *t*-butyl regions integrate to 1:9, consistent with the crystal structure (**Figure S6-S12**).

4. Characterization of 3

X-Ray Crystallography and Twinning:

Diffraction data were collected on a Rigaku SCX-Mini diffractometer (Mercury2 CCD) using graphite-monochromated Mo Kα radiation (λ = 0.71073 Å). Integration was performed with CrysalisPro,[4] and empirical absorption correction was applied using spherical harmonics implemented in the SCALE3 ABSPACK scaling algorithm. All structures were solved by direct methods and refined on F^2 by full matrix least squares using the SHELXTL software package. All thermal ellipsoid plots were generated using Olex2.[5] The groups bound to the diphosphine unit were modeled in two parts, the occupancies were constrained to overall unit occupancy. The non-hydrogen atoms of PART 1 were refined anisotropically and without restraints. However, the non-hydrogen atoms of PART 2 were refined isotropically, and their bond lengths and angles set to refine to the corresponding atoms of PART 1 with SADI commands. The data was refined using the twin law corresponding to racemic twinning. The compound crystallizes in the chiral space

group pair $P4_12_12/P4_32_12$ as a racemic twin. In addition to the crystal being racemic, the structure shows disorder. The major component as refined in $P4_12_12$ is *R,R* while the minor component is *S,S* in a 85:15 relative ratio. These two components also exist in significantly different conformations.

A summary of X-ray data collection and refinement parameters for the compounds is given in **Table S1**. A summary of selected bond lengths and angles for the reported compounds is given in **Table S2**.

NMR Spectra Interpretation:

The ^{31}P and ^{1}H spectra for **3** are not only second-order in nature but suggest **3** possesses hindered rotation about the P-P bond. Given that the crystal is racemic there are equal proportions of (*R*,*R*) and (*S*,*S*) enantiomers overall, even though each takes its turn being the minor component of one of the , the minor component seen in the crystal structure is a conformer, distinguished from the major component by the significantly different rotational orientation of its substituent groups about the phosphorus atoms, a situation which gives rise to two sets of overlapping signals in the ^{1}H-NMR spectrum with the major envelope for the P-H shift centered at 4.81 ppm and the minor component centered at 4.73 ppm (**Figures S6-S8**). The minor conformer has its *t*-butyl groups eclipsed while the major conformer has them well separated, leading to the differing P-H environment. Importantly, the racemic nature of the crystal makes the (*R,R*) designation for the major conformer arbitrary. Both enantiomers have equal proportions of the minor conformer.

The ^{31}P spectrum shows a similar pattern to the ^{1}H pattern, however, with only one set of peaks. A ^{1}H-decoupled ^{31}P experiment revealed only one phosphorus signal (Figure **S6**), suggesting that only one phosphorus environment exists. This is consistent with the two conformers having a similar phosphorus environment. Variable temperature ^{31}P and ^{1}H studies of **3** (RT to 80 ^{o}C) were undertaken in attempts to see if coalescence of the ^{1}H patterns was possible. However, the ratio of the two P-H ^{1}H envelopes did not change (Figure **S11-S12**) although the envelopes migrated away from one another. In the phosphorus spectrum, the P signal migrated and appeared to flatten.

Table S1 Selected Crystallographic Data

Compound	$\{Fe(CO)_4P(H)^tBu\}_2$
Empirical Formula	$C_{16}H_{20}Fe_2O_8P_2$
Formula Weight	513.96
Temperature, K	173.15
Wavelength, Å	0.71073
Crystal System	Tetragonal
Space Group	$P4_32_12$
a, Å	10.2458(2)
b, Å	10.2458(2)
c, Å	21.1573(7)
α, °	90.0
β, °	90.0
γ, °	90.0
Volume, $Å^3$	2221.03(13)
Density (calculated), Mg/m^3	1.537
Absorption Coefficient, mm^{-1}	1.487
F(000)	1052.1658
Crystal Size, mm	0.40 x 0.33 x 0.30
Theta Range for Data Collection, °	2.209 to 31.698
Index Ranges	$-15 < h < 14$; $-15 < k < 15$; $-30 < l < 31$
Reflections Collected	38368
Independent Reflections	3741 [R(int) = 0.0295]
Completeness to $2\theta_{Max}$	99.0%
Absorption Correction	Multi-Scan
Flack Parameter	0.51(2)
Max and Min. Transmission	1.000 and 0.197
Refinement Method	Full-Matrix Least Squares on F^2
Data / restraints / parameters	3706 / 208 / 181
Goodness-of-fit on F^2	1.098
Final R Indices [I>2sigma(I)]	0.0328
R Indices (all data)	0.0365
Largest diff. peak and hole	0.80 and -.43 $e.Å^{-3}$

Table S2. Selected Bond Lengths and Angles:

Parameter	(Å)/(°)
Lengths:	
Fe1-P1A	2.2395(8)
Fe1-P1B	2.325(3)
P1A_a-P1A_b	2.2410(13)
P1B_a-P1B_b	2.428(7)
Angles:	
Fe1-P1A_a-P1A_b	119.92(3)
Fe1-P1B_a-P1B_b	94.0(2)

5. ^{1}H and ^{31}P Spectra for Compound 3

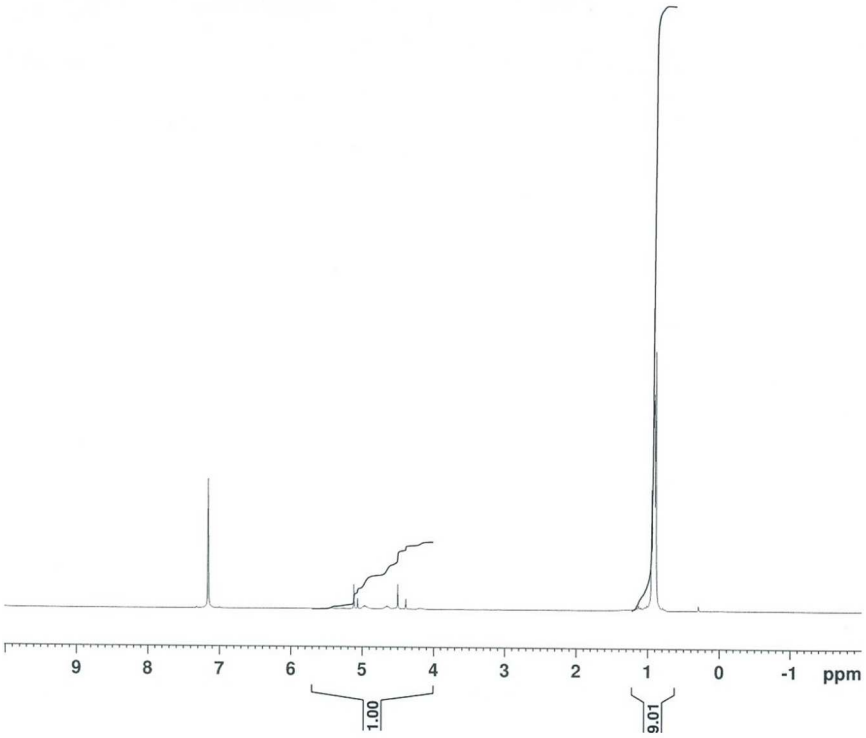

Figure S6. Full ^{1}H Spectrum for **3**

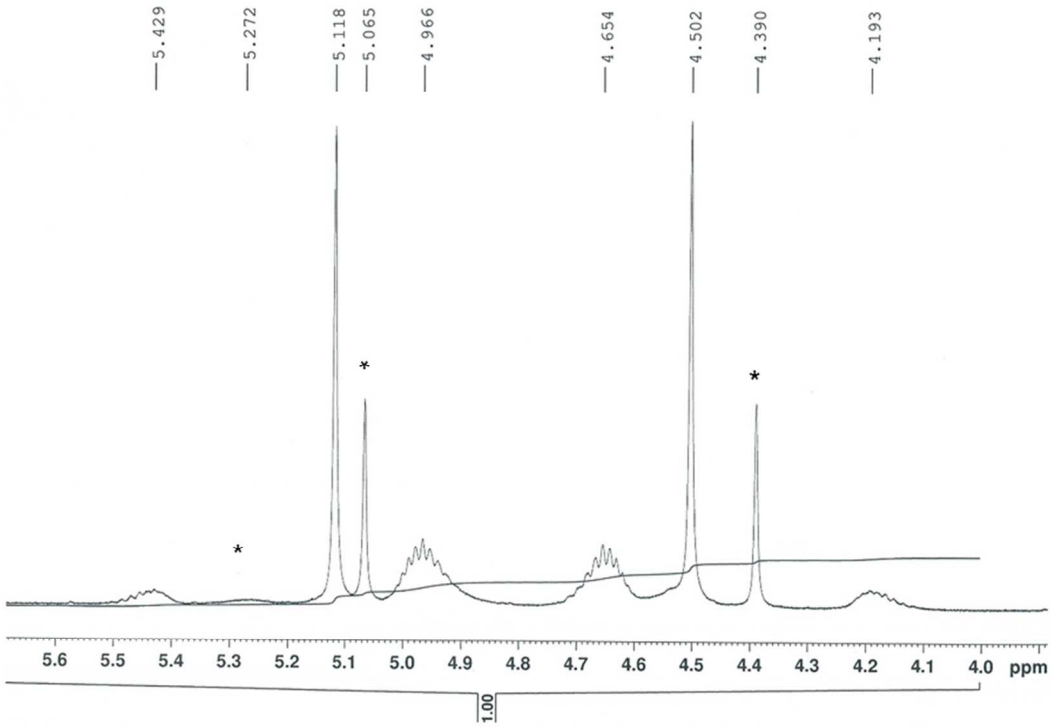

Figure S7. ^{1}H Spectrum for **3** in the P-H region. * belong to the second conformer.

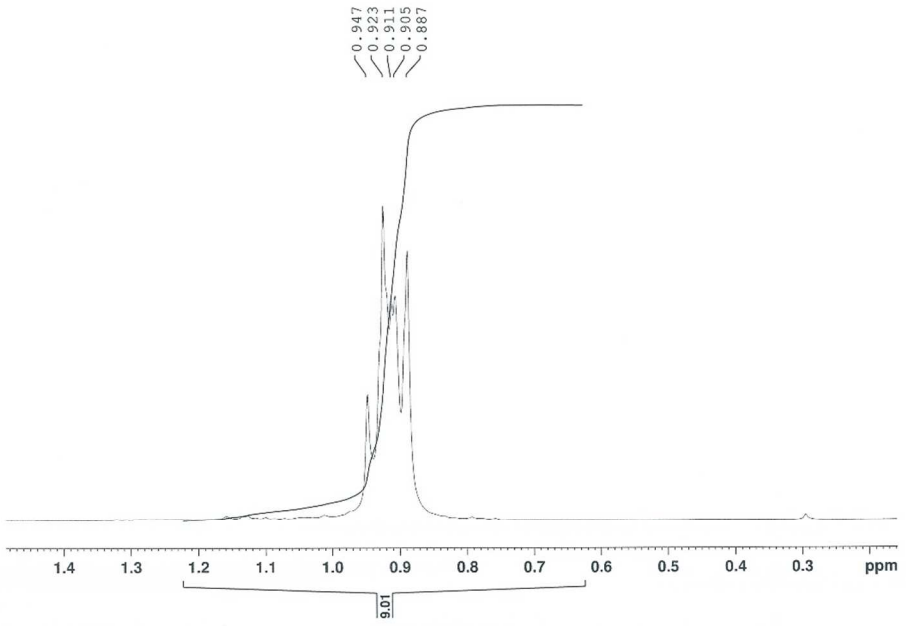

Figure S8. ^{1}H spectrum of **3** in the *t*-butyl region. (overlap of two isomers)

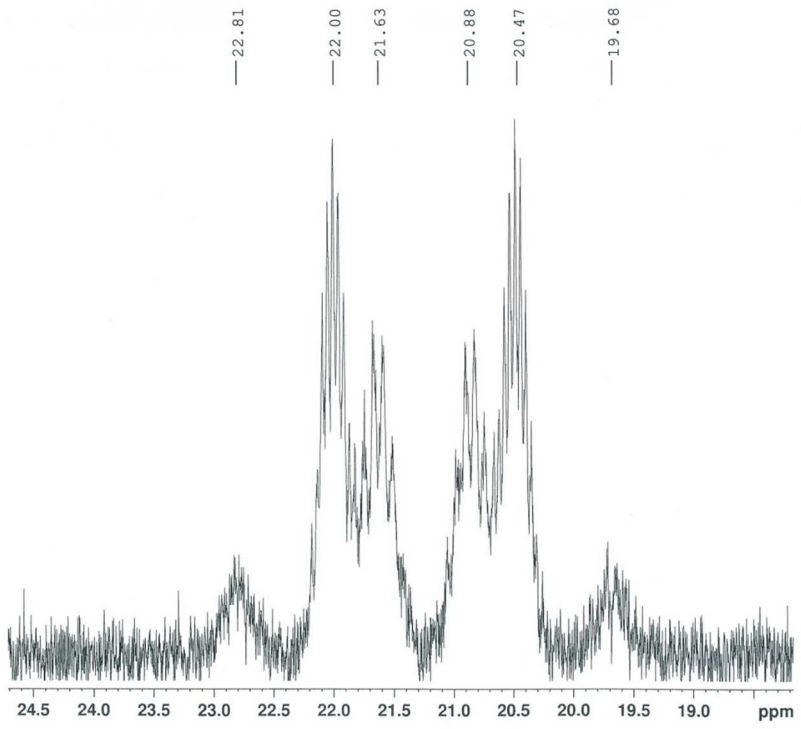

Figure S9. ^{31}P-NMR spectrum of Compound **3**.

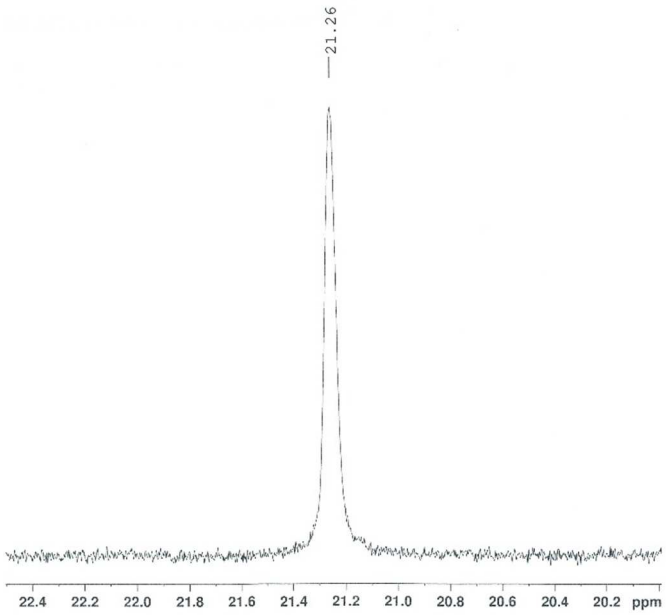

Figure S10. Proton-decoupled ^{31}P-NMR spectrum of Compound **3**

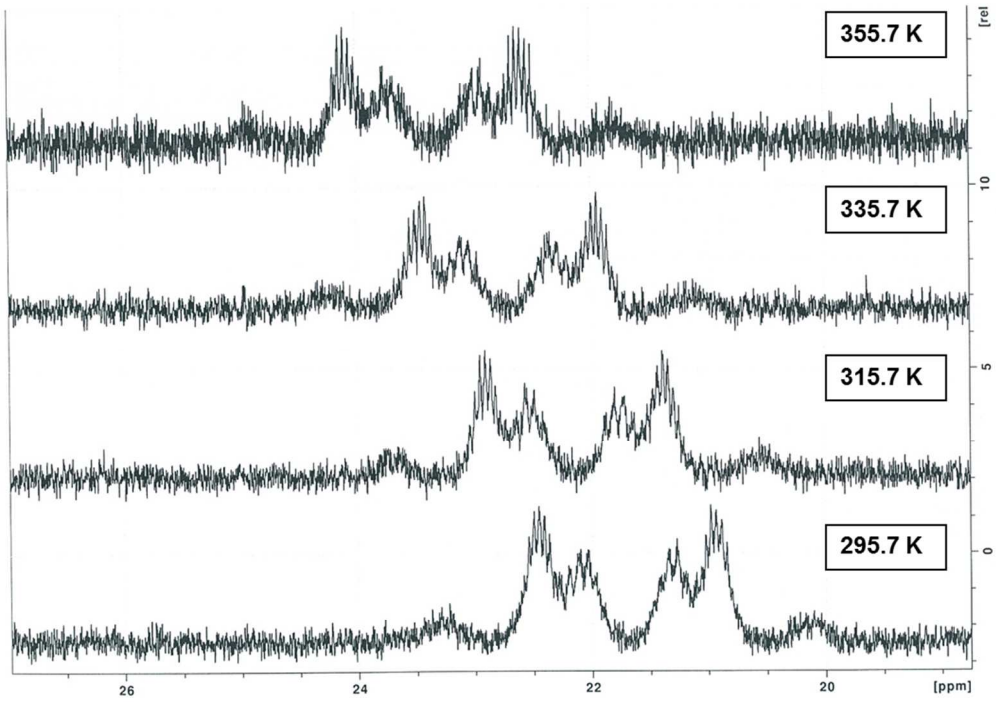

Figure S11. VT ^{31}P-NMR spectrum of Compound **3**

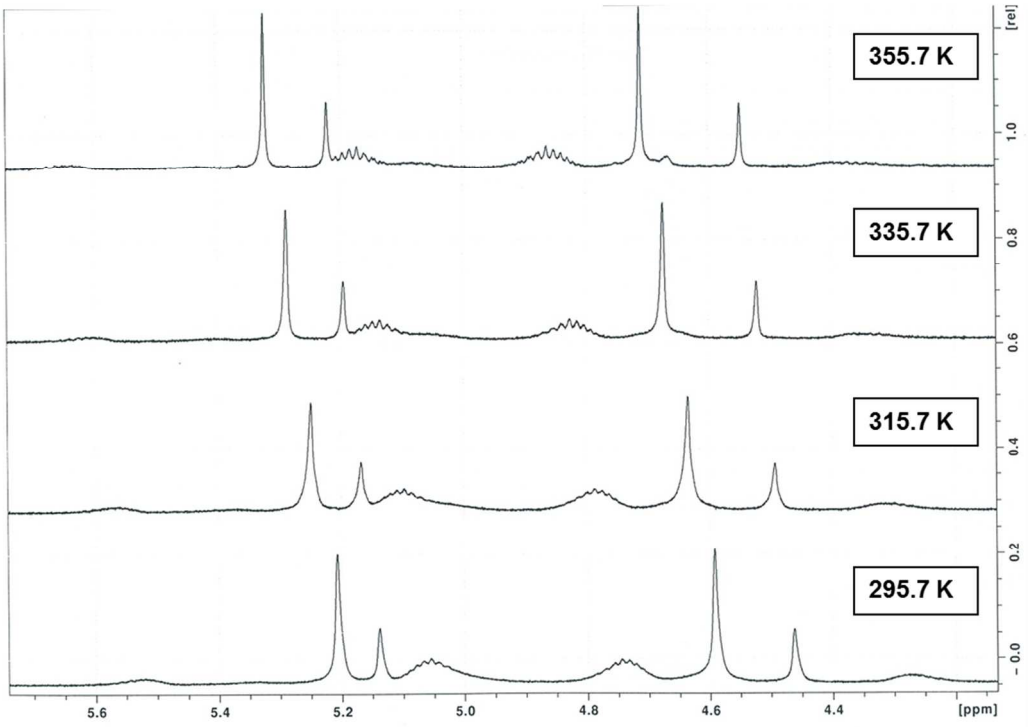

Figure S12. VT ^{1}H-NMR spectrum of Compound **3** in the P-H region

6. ESI-MS Data for Compound 3

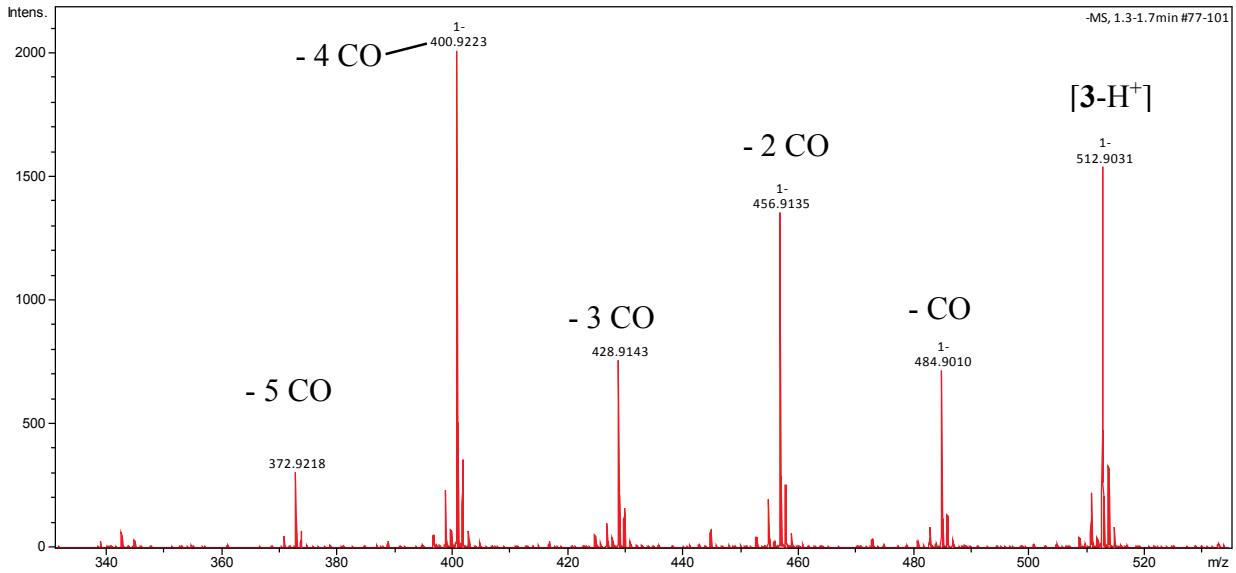

Figure S13. Full spectrum.

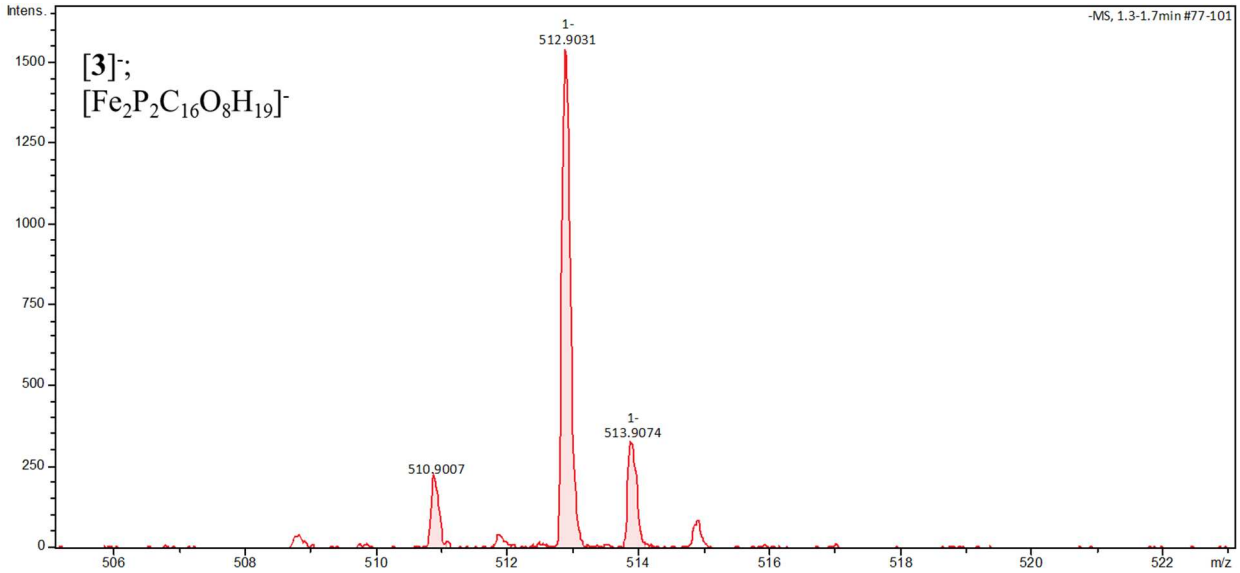

Figure S14. Principal Peak (Experimental).

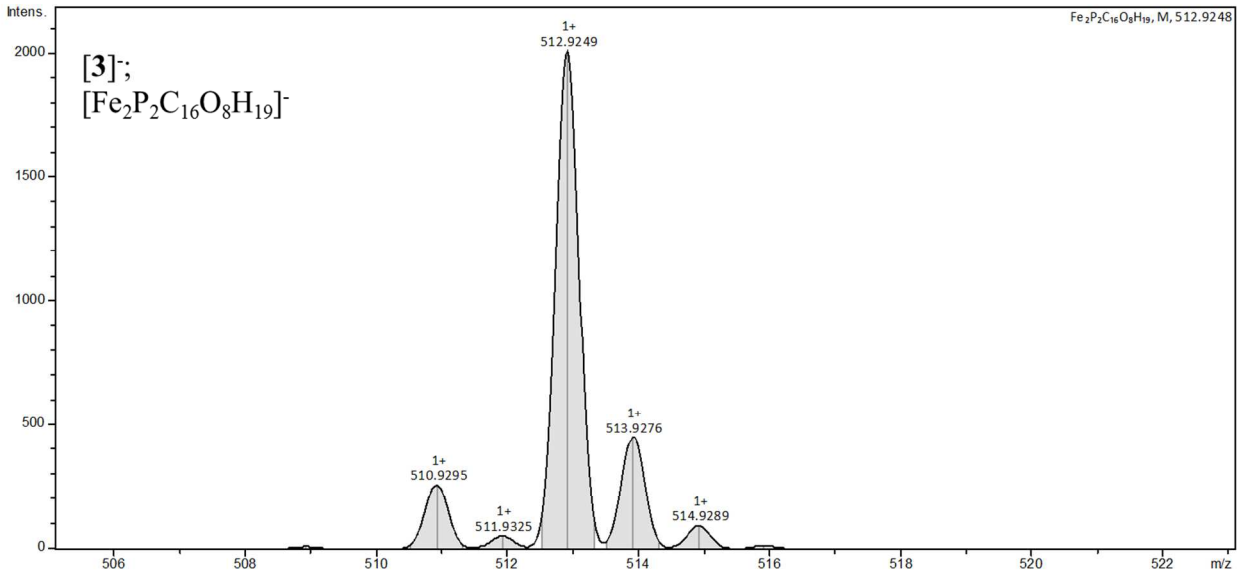

Figure S15. Principal Peak (Simulated Pattern).

7. SEM Images of the Produced Materials:

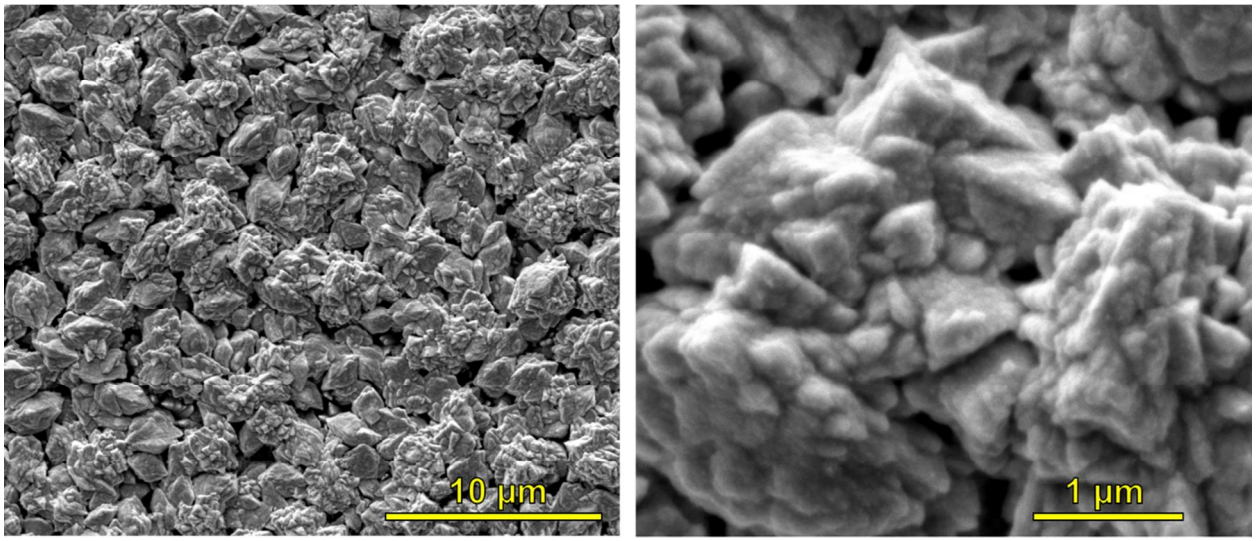

Figure S16. SEM Images of FeP/Fe_2P mixture on quartz at two magnifications.

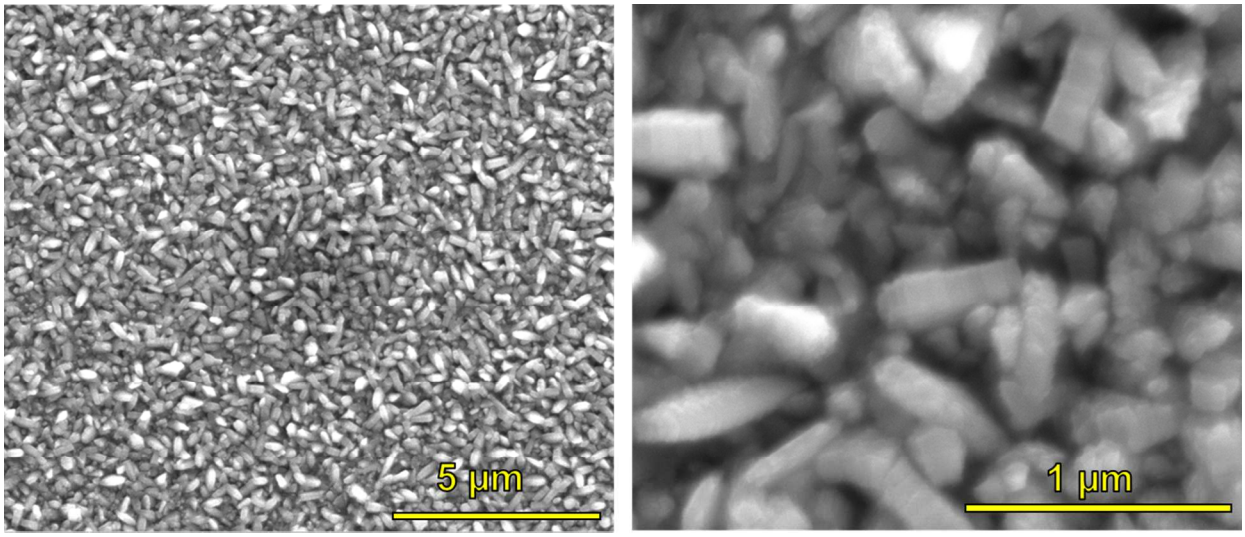

Figure S17. SEM Images of FeP from Precursor **2** on quartz at two magnifications

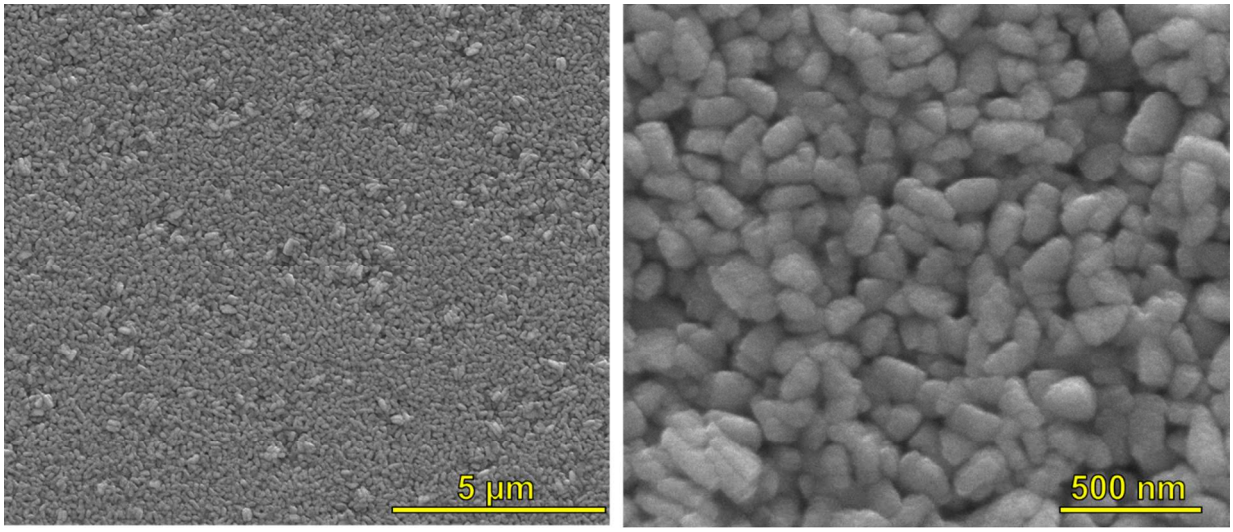

Figure S18. SEM Images of FeP from precursor **3** on quartz at two magnifications.

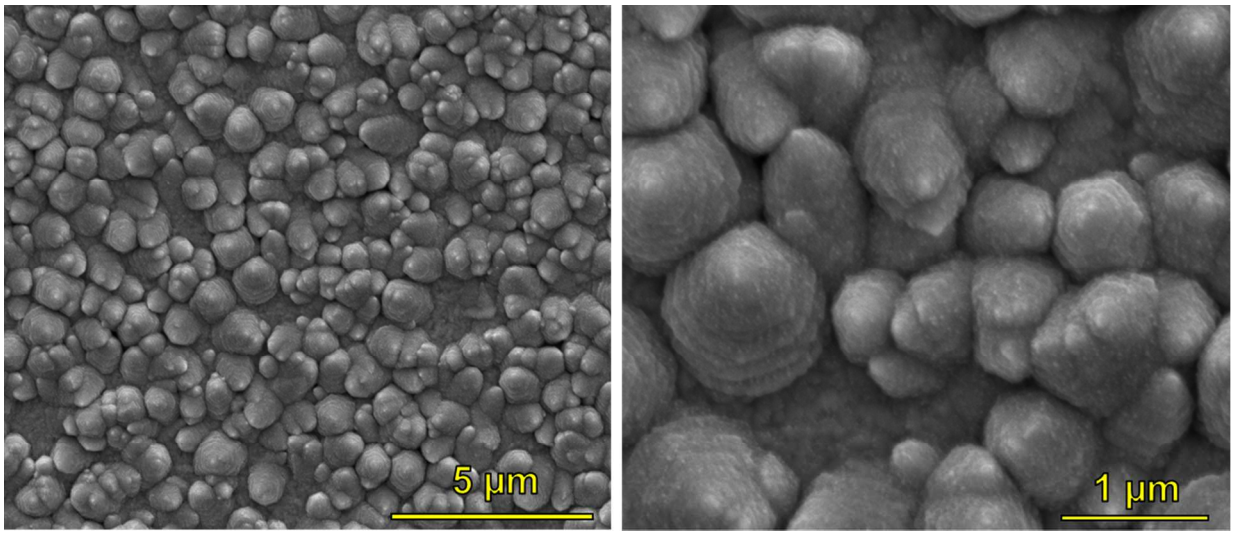

Figure S19. SEM Images of Fe_2P on quartz at two magnifications.

8. Powder X-Ray Diffraction Spectra of the Produced Materials:

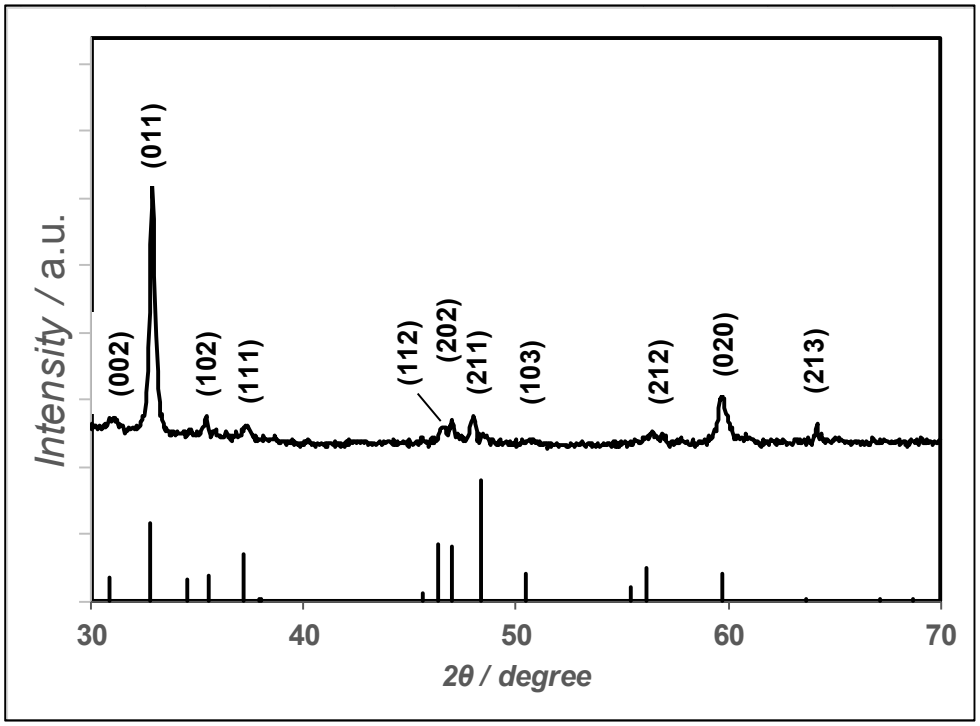

Figure S20. PXRD of FeP on Quartz from precursor **3**.

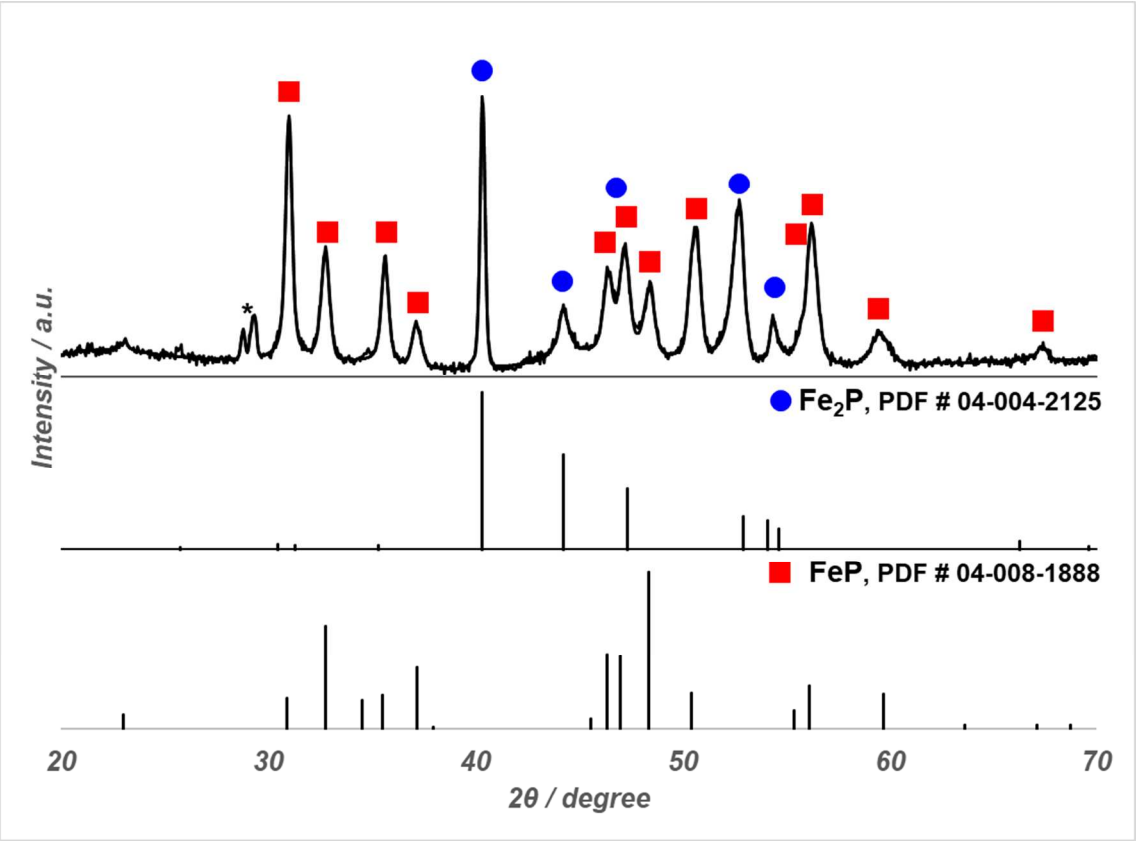

Figure S21. XRD Pattern of FeP/Fe_2P mixture on quartz obtained from the CVD of Precursor **1** at 450 ^{o}C. The asterisk denotes two peaks arising from the substrate.

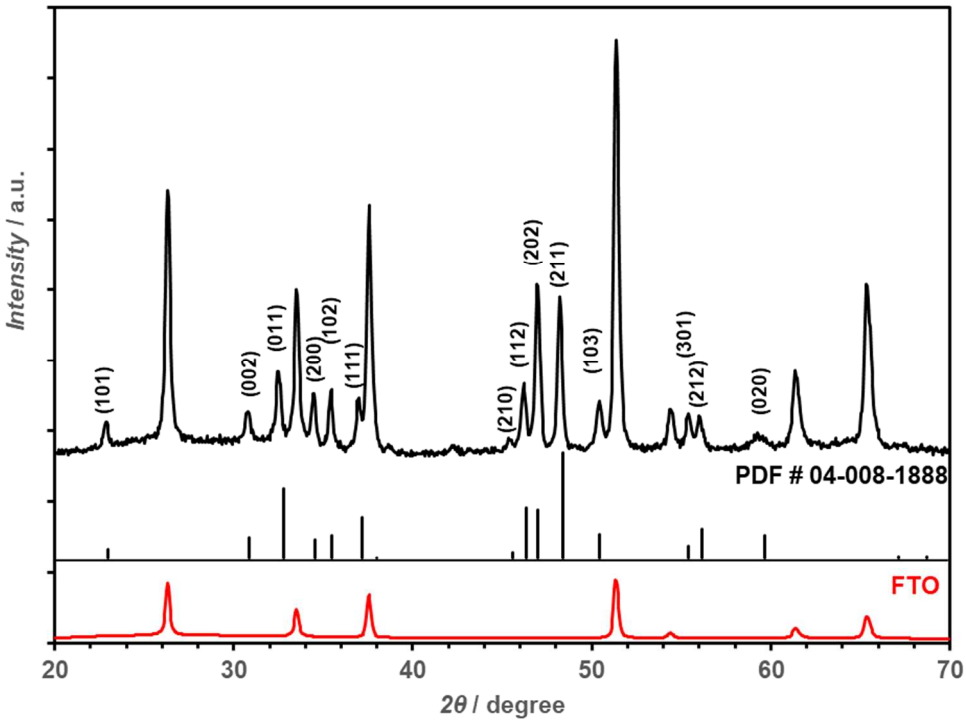

Figure S22. PXRD of FeP on FTO from precursor **2**.

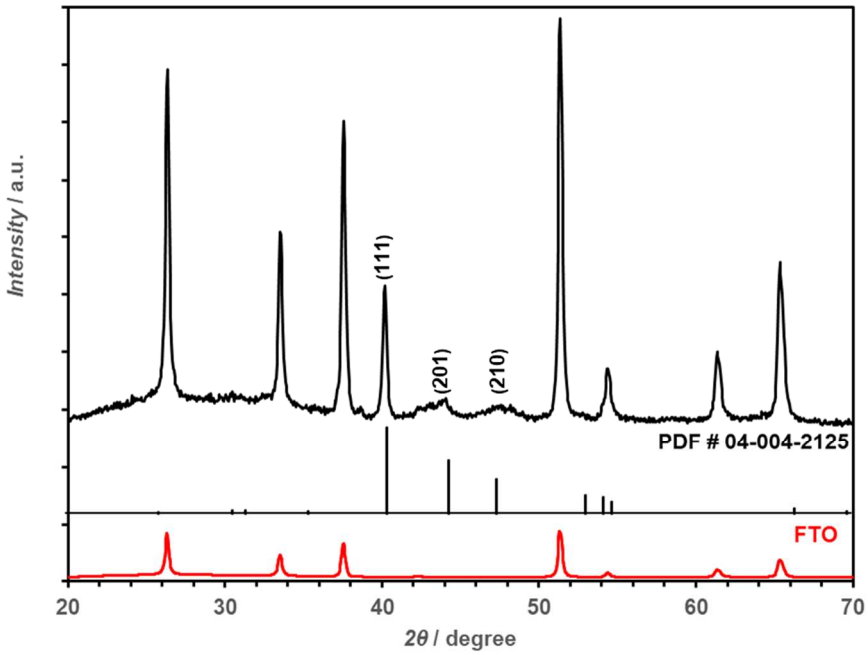

Figure S23. PXRD of Fe_2P on FTO from precursor **1**.

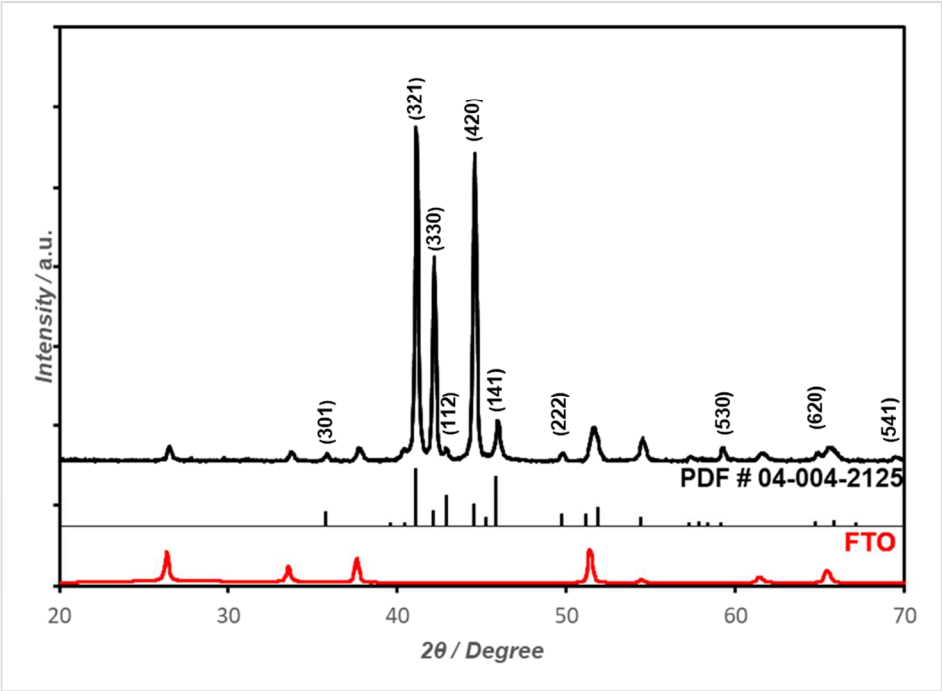

Figure S24. PXRD of Fe_3P on FTO from precursor **4**.

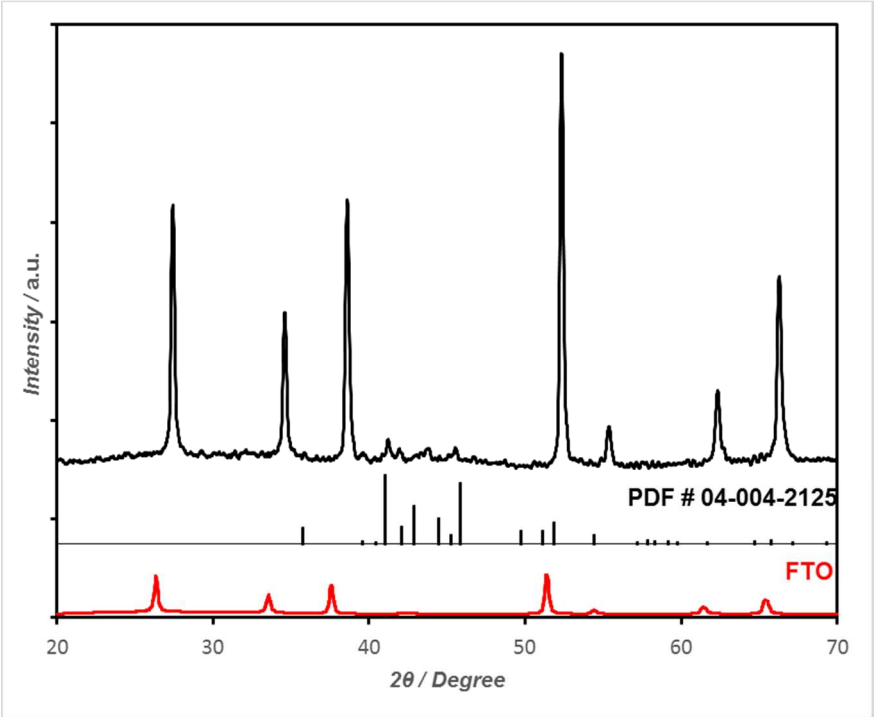

Figure S25. PXRD of unannealed Fe_3P on FTO from precursor **4**.

9. Electrochemical Measurements

Electrochemical measurements of the as-deposited FeP, Fe_2P and Fe_3P films were conducted on a 263A Princeton Applied Research (PAR) potential/galvanostat instrument in a three-electrode setup with Ag|AgCl and Pt plate as the reference electrode, and counter electrode, respectively. The electrolyte solution was 0.5 M H_2SO_4 which was bubbled with N_2 gas for 30 min before use. Linear sweep voltammetry (LSV) was carried out at a scan rate of 5 mV/s for the polarization curves. Electrochemical impedance spectroscopy (EIS) was performed at an AC amplitude of 10 mV in a frequency range of 100000 Hz to 10 mHz at pre-set overpotentials. IR correction was made using the equivalent series resistance from the Nyquist plots in EIS measurements. Before use, the samples were wired using copper wire with silver paste. Epoxy was used to cover the silver paste and the sample leaving an exposed area of 0.5 cm^2. Cyclic voltammetry (CV) was performed at different scan rates in the non-Faradaic reaction potential range to derive the electrochemical double-layer capacitance for the calculation of electrocatalytically active surface area (ECSA). The potential versus that of reversible hydrogen electrode (RHE) was calculated with reference to Ag|AgCl according to the Nerst equation: $E_{RHE} = E_{Ag|AgCl} + 0.059 \times 0.3 + E_o$, where E_{RHE} is the potential vs RHE, $E_{Ag|AgCl}$ is the measured potential vs Ag|AgCl, and $E^o = 0.2$ V at 25 ^oC. The long-term stability was evaluated by chronoamperometry measurement at overpotential of 120 mV. The Faradaic efficiency was obtained by comparing the amount of produced H_2 at the electrode with the amount of calculated H_2 according to current. The produced H_2 was analyzed by a gas chromatography (GC) equipped with a thermal conduction detector (TCD) with Ar as the carrier gas, which was calibrated with H_2 in advance.

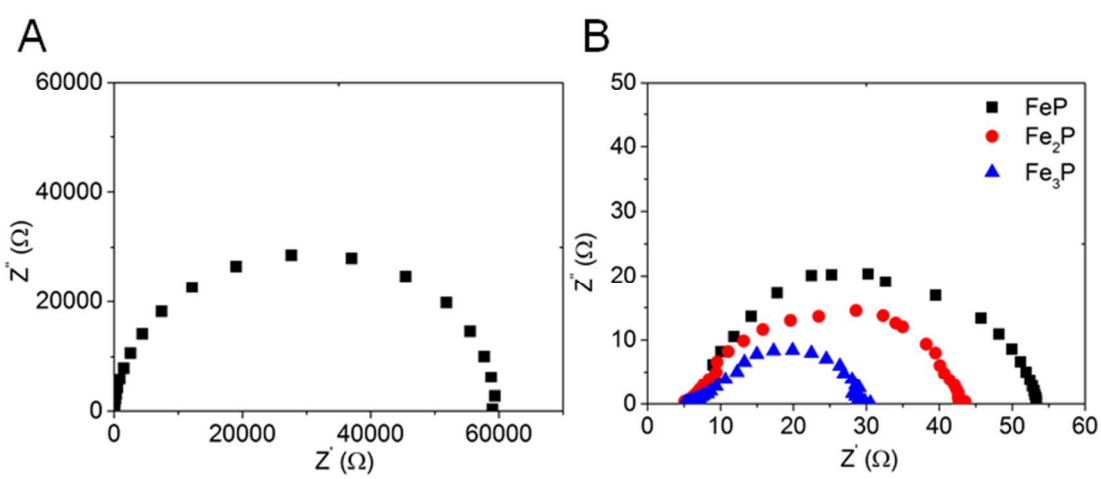

Figure S26. Nyquist plots of bare FTO, FeP, Fe_2P and Fe_3P electrodes at the same overpotential of 160 mV.

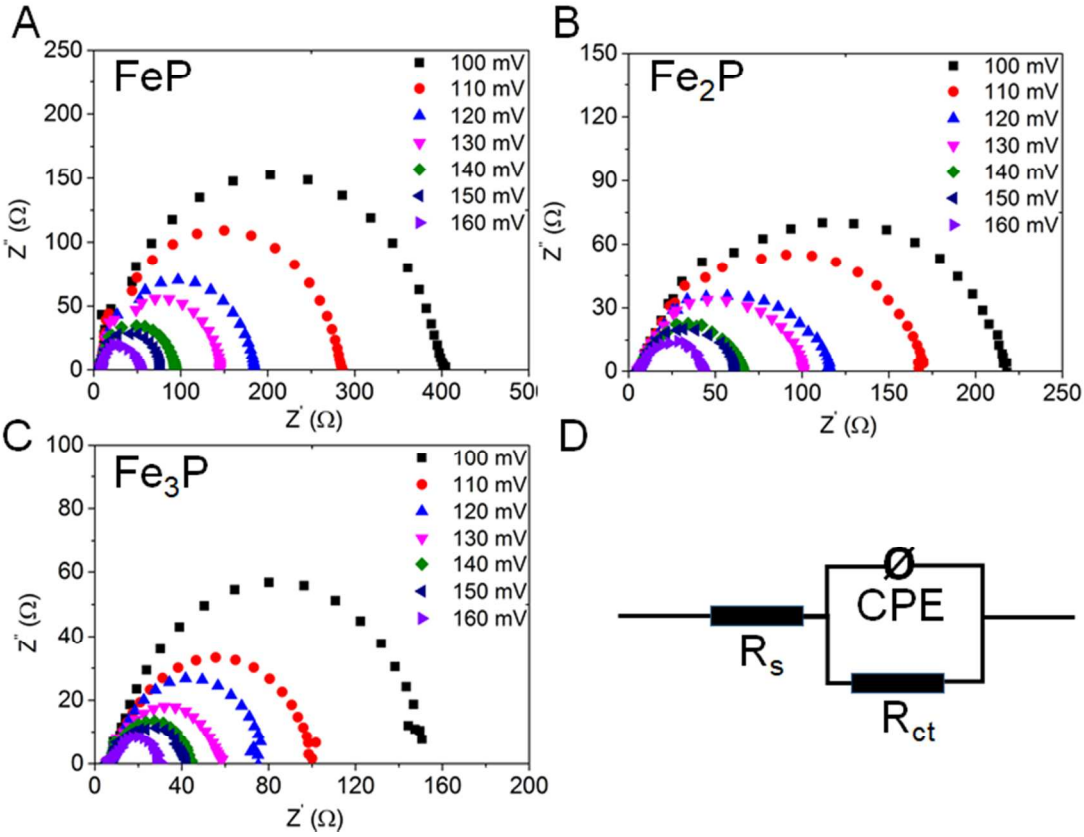

Figure S27. The Nyquist plots of (A) FeP, (B) Fe_2P and (C) Fe_3P electrode at different overpotentials. (D) The equivalent circuit for the Nyquist plots, where R_s, *CPE* and R_{ct} are the equivalent series resistance, constant phase element referring to the double-layer capacitance, and the charge transfer resistance, respectively.

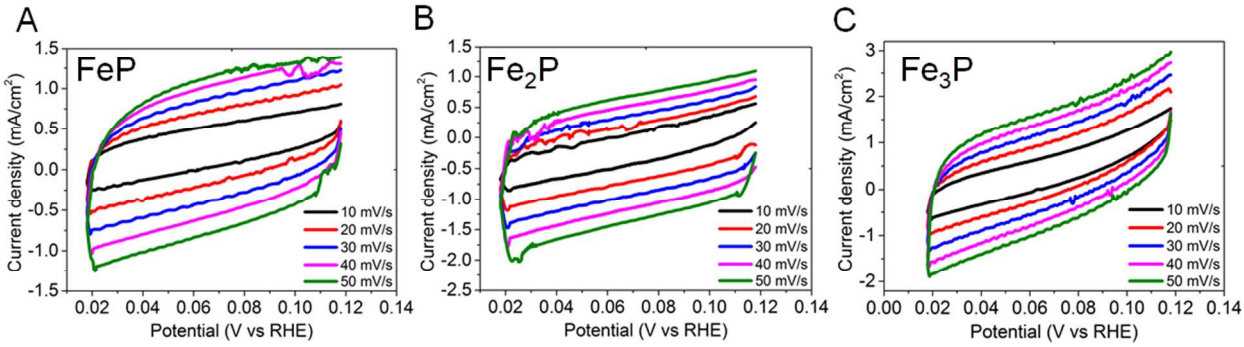

Figure S28. The CV curves recorded in a non-Faradaic reaction potential range of (A) FeP, (B) Fe_2P and (C) Fe_3P.

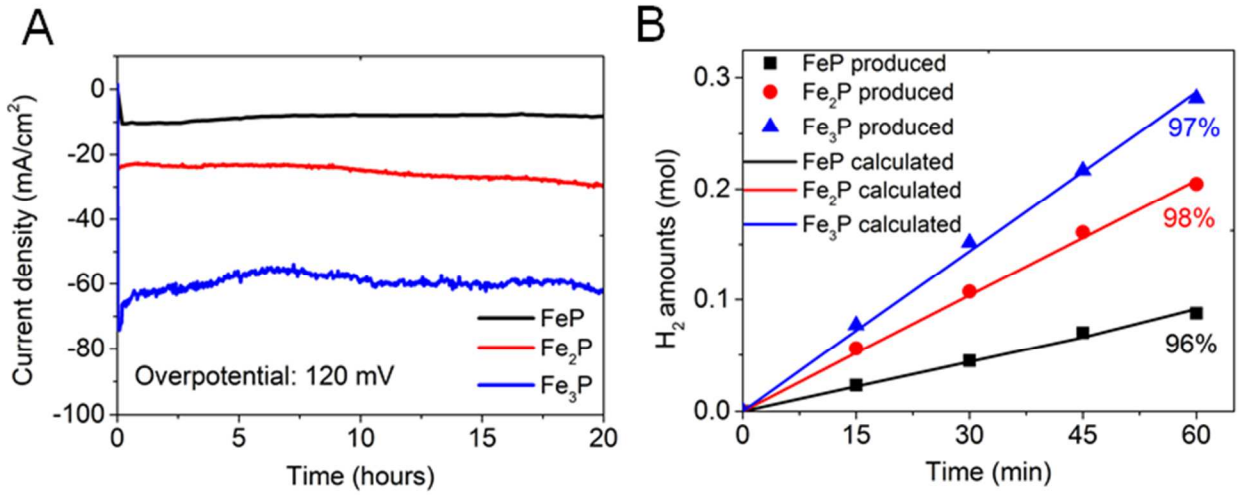

Figure S29. (A) Time dependence of current density under static overpotential of 120 mV for FeP, Fe_2P and Fe_3P for the evaluation of the long-term stability. (B) H_2gas amount versus electrolysis time. The Faradaic efficiency was determined by comparing measured H_2 amount to the amount calculated from the current.

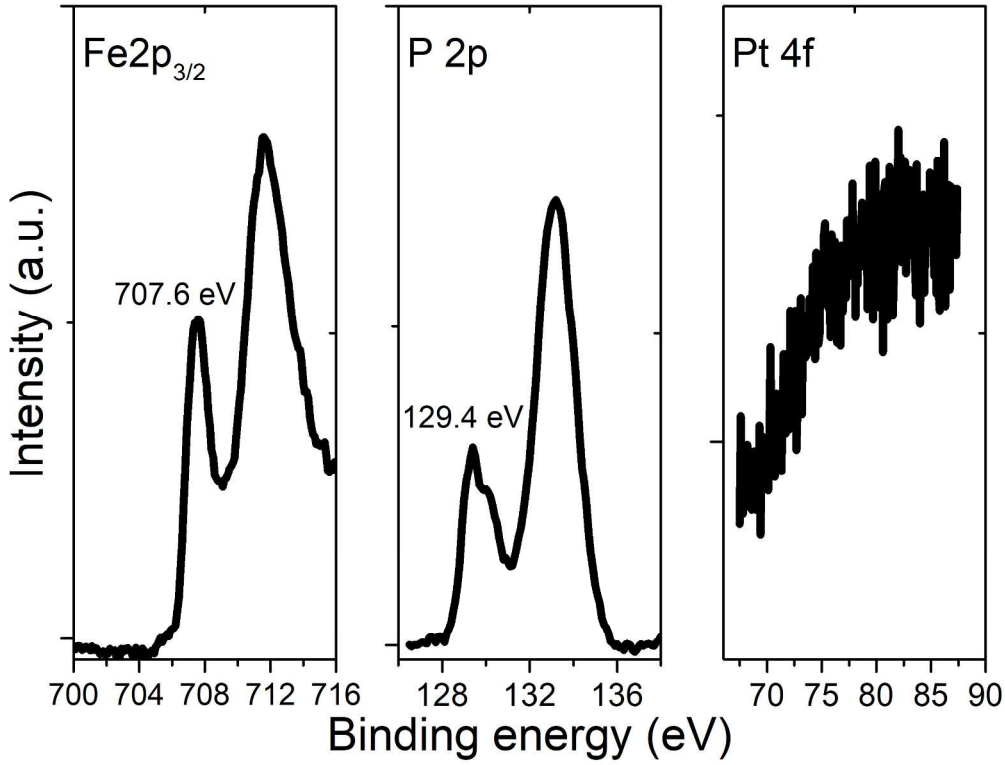

Figure S30. Surface XPS spectra of the Fe_3P film after the HER long-term stability test.

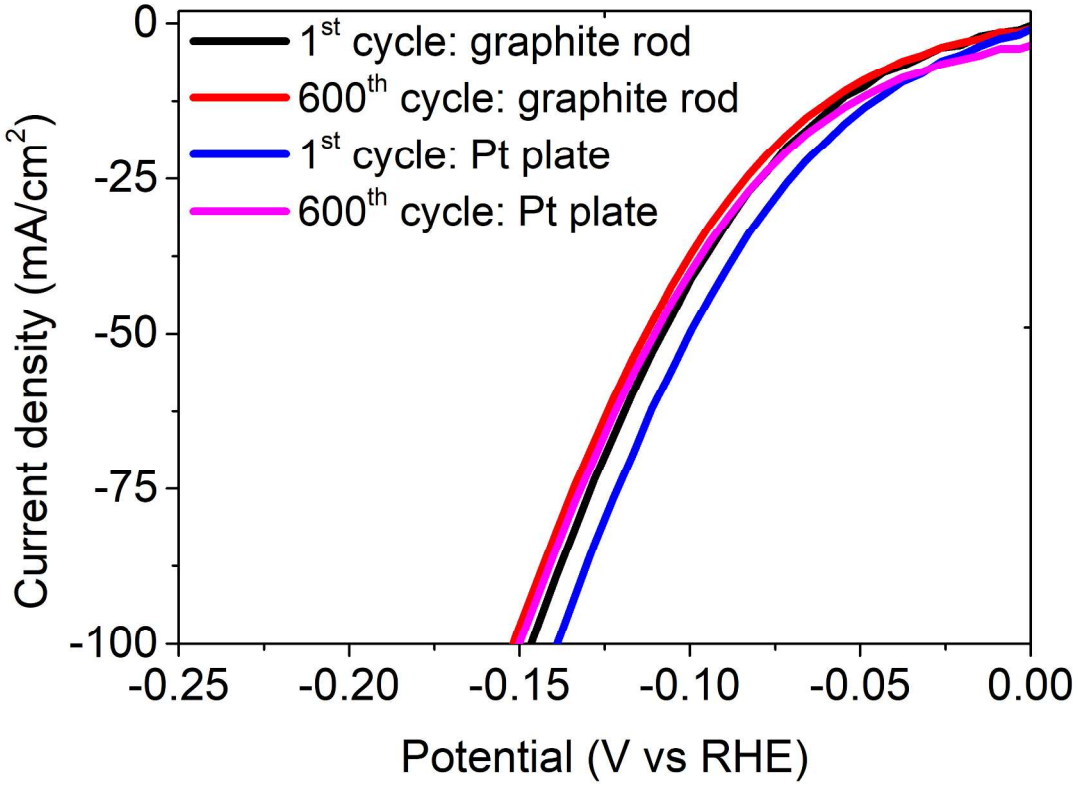

Figure S31. The HER polarization curves of the Fe_3P film electrode on FTO with different counter electrodes at 100 $mV \cdot s^{-1}$ in acid. Two Fe_3P electrodes were separately tested for 600 cycles at 100 $mV \cdot s^{-1}$ in acid with Pt plate and graphite rod as the counter electrode, respectively.

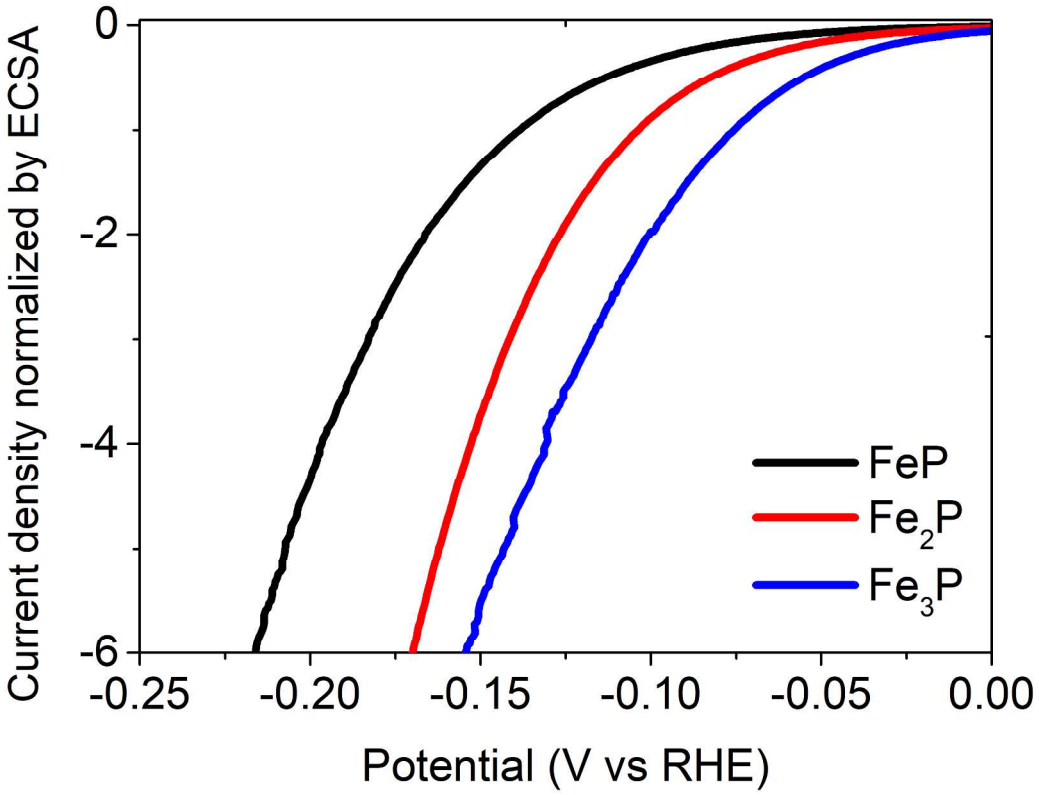

Figure S32. The normalized polarization curves (Figure 5A) by ECSA of the FeP, Fe_2P, and Fe_3P films' electrodes.

Table S4. The HER performance comparison of transition metal phosphides in 0.5 M H_2SO_4 solution. The overpotential is defined as the overpotential to reach a current density of 10 $mA \cdot cm^{-2}$. FTO: Fluorine-doped Tin oxide glass; GCE: glass carbon electrode; rGO: reduced graphene oxide.

Catalyst	**Substrate**	**Overpotential (mV)**	**Tafel slope ($mV \cdot dec^{-1}$)**	**Exchange current density ($mA \cdot cm^{-2}$)**	**Ref.**
Fe_3P	**FTO**	**49**	**57**	**1.32**	**This work**
Fe_2P	**FTO**	**83**	**66**	**0.47**	**This work**
FeP	**FTO**	**116**	**76**	**0.24**	**This work**
FeP nanoparticles	Ti	50		0.43	7
FeP nanotubes	Carbon cloth	88	35.5		8
FeP NWs	rGO	107	58.5		9
FeP nanowires	Carbon paper	31	53		10
FeP nanoparticles	GCE	154	65		11
FeP nanowire	Fe foil	96	39	0.17	12
Fe_2P	GCE	88	49		13
Fe_2P	GCE	101	55.2		14
Fe_2P	Fe foil	191	55		15
FeP_2 nanowire	Fe foil	61	37	0.55	12
CoP nanoparticle	Ti	75	50		16
Co_xP (x=1-2) NPs	Ti	144	58		17
Co_xP (x = 1-2) NPs	Ti	110	51		18
Cu_3P nanowire	Cu foam	143	67	0.18	19
Ni_2P nanoparticle	GCE	> 100	46	0.033	20

10.Density Functional Theory Calculations

All density functional theory calculations were performed using the Vienna Ab-initio Simulation Package (VASP)[21–23] and interfaced through the Atomic Simulation Environment (ASE).[24] The Bayesian error estimation functional[25,26] was used in conjunction with the projector augmented wave (PAW) method[27] to iteratively solve the Kohn-Sham equations. A plane wave cutoff energy of 500 eV and a Gaussian smearing width $k_B T$ = 0.1 eV was employed to ensure accurate extrapolation to obtain ground state energies. Bulk unit cells of Fe_xP were sampled with a (12 × 12 × 12) Monkhorst-Pack k-point grid and surface facets created from these unit cells were sampled with a (6 × 6 × 1) k-point grid.[28] The surface slabs were separated by a vacuum layer of 15 Å in the z-direction and were corrected for any spurious dipole moments arising from adsorbates present on only one side of the slab.[29] Convergence with respect to k-point grid and vacuum spacing was confirmed for all models and all unconstrained atoms in the models were relaxed using a force convergence criterion of 0.02 eV/Å.

Table S5: Bulk unit cells and optimized lattice parameters of Fe_3P, Fe_2P and FeP

Iron Phosphide	Unit Cell	Lattice Parameters
Fe_3P	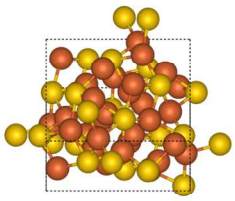	Crystal System: Tetragonal a = b = 9.07 Å c = 4.39 Å
Fe_2P	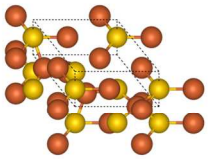	Crystal System: Hexagonal a = 5.82 Å b = 5.04 Å c = 3.42 Å
FeP	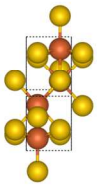	Crystal System: Orthorhombic a = 3.04 Å b = 5.16 Å c = 5.77 Å

The primitive unit cells of Fe_3P, Fe_2P and FeP were obtained from the Materials Project database[30] and were optimized for use with the BEEF-vdW functional and

other calculation parameters chosen in this work. The optimized lattice parameters and bulk unit cell visualizations for all three materials are given in **Table S5** and are in good agreement with those obtained from the characterization done in this work.

The existence of a diverse range of surface terminations under electrocatalytic conditions renders an exhaustive search of active surface facet intractable. Therefore, we employed the Bravais-Friedel-Donnay-Harker (BFDH) crystal morphology algorithm[31] to obtain predictions of exposed surface facets based only on the lattice parameters of the primitive unit cells. Based on these predictions, the (100) facet for Fe_3P, the (100) and (001) facets of Fe_2P and the (100) and (011) facets of FeP were further investigated. Kibsgaard and coworkers[32] concluded that the P-terminated FeP(011) surface facet was an HER active surface termination. The same surface was used in the work of Chung et al.[33] and we considered it as additional surface to keep a common reference point to prior work. All surfaces were modeled as (2 × 2) or (3 × 2) surface unit cells with similar total surface area per unit cell and 4-layer equivalents along the *z*-direction. The adsorbates and the top half of the surfaces were unconstrained and allowed to relax to their ground state geometries. Upon selection of surface facets, the surface formation energies were calculated and are provided along with the surface visualizations in **Table S6**. Cleavage of Fe_2P along the (001) direction results in the formation of bilayered and asymmetrically terminated slabs. Therefore, the surface formation energy was calculated as per the procedure outlined in the work of Santos-Carballal and coworkers.[34] Similarly, the (011) FeP surface facet is also bilayered in nature can be exposed as either Fe-terminated or P-terminated surfaces.

Table S6: Surface facets and formation energies for the facets investigated in this work.

Iron Phosphide	Exposed surface facet and surface formation energy ɣ
Fe_3P	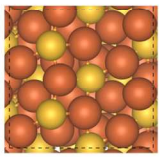 (100) $ɣ_{(100)}$ = 0.14 eV/Å^2
Fe_2P	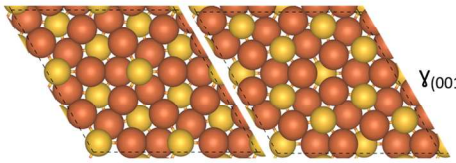 (001)-Fe_3P_2-t (001)-Fe_3P-t $ɣ_{(001)}$ = 0.09 eV/Å^2 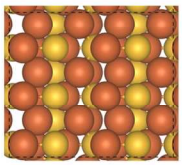 (100) $ɣ_{(100)}$ = 0.14 eV/Å^2
FeP	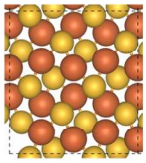 (100) $ɣ_{(100)}$ = 0.12 eV/Å^2 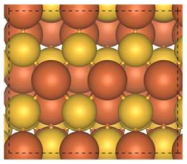 (011)-Fe-t $ɣ_{(011)\text{-Fe-t}}$ = 0.14 eV/Å^2 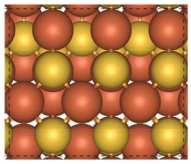 (011)-P-t $ɣ_{(011)\text{-P-t}}$ = 0.11 eV/Å^2

The aforementioned surfaces of Fe_3P, Fe_2P and FeP were populated with hydrogen atoms to determine preferred binding sites. This was done by adsorbing hydrogen atoms based on a grid on select surface facets. All relaxed surfaces show minor rearrangement to form distinct Fe-Fe bridge sites, which are the preferred adsorption sites for hydrogen. The binding energy for hydrogen was calculated in reference to a clean relaxed slab and a gas phase hydrogen molecule in a box of dimensions 12 × 12 × 12 Å, sampled at the **Γ**-point. All other input parameters were identical to those in surface calculations, except for the Gaussian smearing width $k_B T$, which was lowered to 0.01 eV. The integral energy of adsorption of hydrogen was calculated according to **equation (1)**

$$\Delta E_H(n) = E_{slab+n\times H} - \left(E_{slab,clean} + n \times \frac{1}{2} E_{H_2,gas}\right) \quad (1),$$

$$\Delta G_H(n) = \Delta E_H(n) + \Delta ZPE(n) - T\Delta S(n) \quad (2),$$

where n is the number of adsorbed hydrogen atoms, and E is the electronic energy calculated from DFT.

The free energy of adsorption $\Delta G_H(n)$ is given by **equation (2)**, where the entropy (S) and the zero-point energy (ZPE) contributions were calculated from a normal mode frequency analysis in the harmonic limit for slabs, and at the ideal gas limit for hydrogen gas at standard state (100 kPa and 300 K). The ZPE and S contributions were assumed to increase monotonically with increasing number of hydrogen atoms adsorbed in each distinct adsorption geometry. The differential free energy of hydrogen adsorption ($\frac{\partial \Delta G_H}{\partial n_H}$) has been shown to be an excellent descriptor of the intrinsic HER activity of a surface[35,36] and can be estimated as the change in ΔG_H of the surface due to the adsorption of an additional H atom on the catalyst surface. This is given by **equation 3**,

$$\frac{\partial \Delta G_H}{\partial n_H} = \Delta G_H(n) - \Delta G_H(n-1) \qquad (3)$$

11.Hydrogen Binding Contours

The hydrogen binding preferences were carefully studied on the Fe_3P (100), Fe_2P (100), FeP (011) Fe- and P-terminated and the FeP (100) surfaces. While other iron phosphides facets were included in computing the coverage-dependent differential $\Delta G_H \left(\frac{\partial \Delta G_H}{\partial n_H}\right)$ in the main text, we limited this set of calculations to compensate for the high computational expense incurred when calculating 100 binding energies for each facet. Hydrogen atoms were adsorbed onto the surface of the catalyst at pre-determined, regularly spaced x and y coordinates, as seen in **Figure S34**. While this image visualizes all hydrogen atoms in their respective grid positions, the actual relaxation was performed with only one atom at a time. The laterally constrained hydrogen adsorbate was allowed to move in the (z) direction normal to the surface. In addition, the top half of the surface is allowed to relax as in all other calculations performed in this work. A force convergence criterion of 0.02 eV/Å was used to ensure strict geometric convergence.

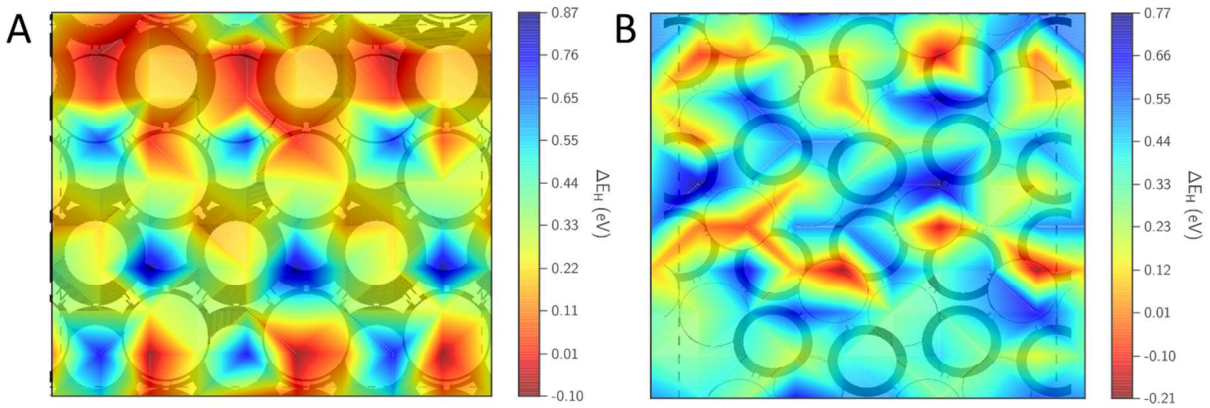

Figure S33: Contours of H binding strength on the surfaces of a) P-terminated $FeP_{P\text{-}t}$ (011) and b) FeP (100). Fe atoms are depicted with thick boundaries, while P atoms are depicted with thin boundaries. Red areas indicate strong binding, while blue represents areas of weak binding.

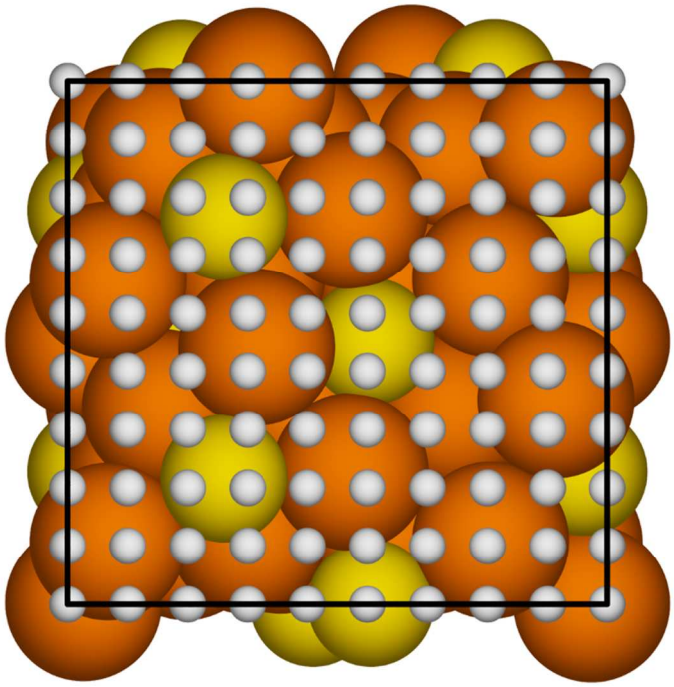

Figure S34: Regular grid of 100 H atoms fixed in their (x, y) Cartesian coordinates on the Fe_3P (100) surface.

12. Calculated Differential Gibbs Free Energy of Adsorption

The differential Gibbs free energy of adsorption $\left(\frac{\partial \Delta G_H}{\partial n_H}\right)$ as a function of the number of hydrogen atoms adsorbed per unit cm^2 of catalyst surface area for all surfaces are given in **Tables S7** to **S13**.

Table S7: Fe_3P (100)

n_H	ΔE	ΔZPE	TΔS	ΔG	ΔE_{net}	ΔE_{diff}	ΔG_{net}	ΔG_{diff}	n_H/cm^2
	eV per H adsorbed				(eV)	(eV)	(eV)	(eV)	
1	-0.59	0.03	-0.20	-0.37	-0.59	-0.59	-0.37	-0.37	1.26E+14
2	-0.60	0.03	-0.20	-0.37	-1.19	-0.60	-0.74	-0.37	2.51E+14
3	-0.51	0.03	-0.19	-0.29	-1.69	-0.51	-1.03	-0.29	3.77E+14
4	-0.46	0.02	-0.19	-0.24	-2.15	-0.46	-1.27	-0.24	5.02E+14
5	-0.31	0.02	-0.19	-0.10	-2.46	-0.31	-1.36	-0.10	6.28E+14
6	-0.22	0.02	-0.19	0.00	-2.68	-0.22	-1.36	0.00	7.53E+14
7	-0.19	0.03	-0.19	0.03	-2.87	-0.19	-1.33	0.03	8.79E+14
8	-0.17	0.03	-0.19	0.06	-3.04	-0.17	-1.27	0.06	1.00E+15
9	-0.09	0.03	-0.19	0.13	-3.13	-0.09	-1.14	0.13	1.13E+15
10	-0.03	0.03	-0.19	0.19	-3.16	-0.03	-0.95	0.19	1.26E+15
11	0.00	0.03	-0.19	0.22	-3.16	0.00	-0.73	0.22	1.38E+15
12	0.02	0.03	-0.19	0.24	-3.15	0.02	-0.49	0.24	1.51E+15

Area of surface unit cell = 79.68 $Å^2$

Table S8: Fe_2P (001) - Fe_3P terminated surface

n_H	ΔE	ΔZPE	TΔS	ΔG	ΔE_{net}	ΔE_{diff}	ΔG_{net}	ΔG_{diff}	n_H/cm^2
	eV per H adsorbed				(eV)	(eV)	(eV)	(eV)	
1	-0.28	0.01	-0.19	-0.07	-0.28	-0.28	-0.07	-0.07	8.51E+13
2	-0.30	0.01	-0.19	-0.09	-0.57	-0.30	-0.16	-0.09	1.70E+14
3	-0.31	0.01	-0.19	-0.11	-0.88	-0.31	-0.27	-0.11	2.55E+14
4	-0.33	0.01	-0.19	-0.13	-1.22	-0.33	-0.39	-0.13	3.41E+14
5	-0.22	0.00	-0.19	-0.03	-1.44	-0.22	-0.42	-0.03	4.26E+14
6	-0.16	-0.01	-0.19	0.02	-1.60	-0.16	-0.41	0.02	5.11E+14
7	-0.12	-0.01	-0.18	0.05	-1.72	-0.12	-0.36	0.05	5.96E+14
8	-0.02	-0.02	-0.18	0.15	-1.74	-0.02	-0.21	0.15	6.81E+14

Area of surface unit cell = 117.46 $Å^2$

Table S9: Fe_2P (001) - Fe_3P_2 terminated surface

n_H	ΔE	ΔZPE	TΔS	ΔG	ΔE_{net}	ΔE_{diff}	ΔG_{net}	ΔG_{diff}	n_H/cm^2
	eV per H adsorbed				(eV)	(eV)	(eV)	(eV)	
1	-0.82	0.03	-0.20	-0.60	-0.82	-0.82	-0.60	-0.60	8.51E+13
2	-0.73	0.03	-0.20	-0.51	-1.56	-0.73	-1.11	-0.51	1.70E+14
3	-0.69	0.03	-0.20	-0.47	-2.25	-0.69	-1.58	-0.47	2.55E+14
4	-0.68	0.03	-0.20	-0.45	-2.93	-0.68	-2.04	-0.45	3.41E+14
5	-0.49	0.03	-0.20	-0.27	-3.42	-0.49	-2.30	-0.27	4.26E+14
6	-0.43	0.03	-0.20	-0.21	-3.85	-0.43	-2.51	-0.21	5.11E+14
7	-0.35	0.03	-0.20	-0.13	-4.20	-0.35	-2.64	-0.13	5.96E+14
8	-0.29	0.03	-0.20	-0.06	-4.49	-0.29	-2.70	-0.06	6.81E+14
9	-0.26	0.03	-0.20	-0.03	-4.75	-0.26	-2.73	-0.03	7.66E+14
10	-0.23	0.03	-0.20	0.00	-4.98	-0.23	-2.74	0.00	8.51E+14
11	-0.21	0.03	-0.20	0.02	-5.19	-0.21	-2.72	0.02	9.36E+14
12	-0.19	0.03	-0.20	0.04	-5.38	-0.19	-2.68	0.04	1.02E+15

Table S10: Fe_2P (100)

n_H	ΔE	ΔZPE	TΔS	ΔG	ΔE_{net}	ΔE_{diff}	ΔG_{net}	ΔG_{diff}	n_H/cm^2
	eV per H adsorbed				(eV)	(eV)	(eV)	(eV)	
1	-0.41	0.02	-0.19	-0.20	-0.41	-0.41	-0.20	-0.20	8.37E+13
2	-0.42	0.02	-0.19	-0.20	-0.83	-0.42	-0.41	-0.20	1.67E+14
3	-0.42	0.02	-0.19	-0.21	-1.25	-0.42	-0.62	-0.21	2.51E+14
4	-0.41	0.02	-0.19	-0.20	-1.66	-0.41	-0.81	-0.20	3.35E+14
5	-0.40	0.02	-0.19	-0.19	-2.06	-0.40	-1.00	-0.19	4.18E+14
6	-0.39	0.02	-0.19	-0.18	-2.45	-0.39	-1.18	-0.18	5.02E+14
7	-0.30	0.02	-0.19	-0.09	-2.75	-0.30	-1.27	-0.09	5.86E+14
8	-0.23	0.02	-0.19	-0.02	-2.98	-0.23	-1.29	-0.02	6.70E+14
9	-0.15	0.02	-0.19	0.07	-3.14	-0.15	-1.22	0.07	7.53E+14
10	-0.11	0.03	-0.19	0.11	-3.24	-0.11	-1.11	0.11	8.37E+14
11	-0.06	0.03	-0.19	0.16	-3.31	-0.06	-0.95	0.16	9.21E+14
12	-0.05	0.03	-0.19	0.18	-3.35	-0.05	-0.77	0.18	1.00E+15
13	-0.03	0.04	-0.19	0.20	-3.38	-0.03	-0.57	0.20	1.09E+15

Area of surface unit cell = 119.49 $Å^2$

Table S11: FeP (011) – Fe terminated surface

n_H	ΔE	ΔZPE	TΔS	ΔG	ΔE_{net}	ΔE_{diff}	ΔG_{net}	ΔG_{diff}	n_H/cm^2
	eV per H adsorbed				(eV)	(eV)	(eV)	(eV)	
1	-0.23	0.01	-0.19	-0.03	-0.23	-0.23	-0.03	-0.03	1.42E+14
2	-0.24	0.01	-0.19	-0.04	-0.47	-0.24	-0.06	-0.04	2.83E+14
3	-0.21	0.01	-0.19	-0.01	-0.68	-0.21	-0.07	-0.01	4.25E+14
4	-0.12	0.02	-0.19	0.08	-0.80	-0.12	0.01	0.08	5.66E+14
5	-0.07	0.02	-0.19	0.14	-0.87	-0.07	0.15	0.14	7.08E+14
6	-0.02	0.02	-0.19	0.19	-0.88	-0.02	0.34	0.19	8.49E+14

Area of surface unit cell = 70.64 $Å^2$

Table S12: FeP (011) – P terminated surface

n_H	ΔE	ΔZPE	TΔS	ΔG	ΔE_{net}	ΔE_{diff}	ΔG_{net}	ΔG_{diff}	nH/cm^2
	eV per H adsorbed				(eV)	(eV)	(eV)	(eV)	
1	-0.22	0.03	-0.19	0.01	-0.22	-0.22	0.01	0.01	1.42E+14
2	-0.16	0.03	-0.19	0.07	-0.37	-0.16	0.08	0.07	2.83E+14
3	-0.08	0.03	-0.19	0.14	-0.46	-0.08	0.22	0.14	4.25E+14
4	-0.07	0.04	-0.19	0.16	-0.53	-0.07	0.38	0.16	5.66E+14
5	0.03	0.04	-0.19	0.27	-0.50	0.03	0.64	0.27	7.08E+14
6	0.07	0.05	-0.19	0.30	-0.43	0.07	0.95	0.30	8.49E+14

Area of surface unit cell = 70.64 $Å^2$

Table S13: FeP (100)

n_H	ΔE	ΔZPE	TΔS	ΔG	ΔE_{net}	ΔE_{diff}	ΔG_{net}	ΔG_{diff}	n_H/cm^2
	eV per H adsorbed				(eV)	(eV)	(eV)	(eV)	
1	-0.24	0.08	-0.19	0.03	-0.24	-0.24	0.03	0.03	8.39E+13
2	-0.24	0.08	-0.19	0.03	-0.48	-0.24	0.05	0.03	1.68E+14
3	-0.24	0.08	-0.19	0.03	-0.72	-0.24	0.08	0.03	2.52E+14
4	-0.24	0.08	-0.19	0.03	-0.95	-0.24	0.11	0.03	3.36E+14
5	-0.24	0.08	-0.19	0.02	-1.20	-0.24	0.13	0.02	4.20E+14
6	-0.25	0.08	-0.19	0.02	-1.45	-0.25	0.15	0.02	5.04E+14
7	-0.25	0.08	-0.19	0.01	-1.70	-0.25	0.16	0.01	5.88E+14
8	-0.26	0.08	-0.19	0.01	-1.96	-0.26	0.18	0.01	6.72E+14
9	-0.25	0.07	-0.19	0.02	-2.20	-0.25	0.19	0.02	7.55E+14
10	-0.24	0.07	-0.19	0.02	-2.44	-0.24	0.21	0.02	8.39E+14
11	-0.23	0.06	-0.19	0.02	-2.67	-0.23	0.24	0.02	9.23E+14
12	-0.23	0.06	-0.19	0.03	-2.90	-0.23	0.26	0.03	1.01E+15

Area of surface unit cell = 119.13 $Å^2$

13. References

(1) Colson, A. C.; Whitmire, K. H. Synthesis, Characterization, and Reactivity of the Heterometallic Dinuclear μ-PH_2 and μ-PPhH Complexes $FeMn(CO)_8$(μ-PH_2) and $FeMn(CO)_8$(μ-PPhH). *Organometallics* **2010**, *29*, 4611–4618.

(2) Müller, M.; Vahrenkamp, H. Cluster-Konstruktion: Schrittweiser Aufbau von M_3-RP-Trimetall-Clustern Über P–H-Verbindungen. *Chem. Ber.* **1983**, *116* (6), 2311–2321.

(3) Huttner, G.; Schneider, J.; Mohr, G.; Von Seyerl, J. R—P-Verbrückte Eien-Cluster-Hydride. *J. Organomet. Chem.* **1980**, *191*, 161–169.

(4) *CrysAlisPro*; Rigaku Oxford Diffraction: Yarnton, England, 2015.

(5) Dolomanov, O. V.; Bourhis, L. J.; Gildea, R. J.; Howard, J. a. K.; Puschmann, H. OLEX2: A Complete Structure Solution, Refinement and Analysis Program. *J. Appl. Crystallogr.* **2009**, *42*, 339–341.

(6) Leitner, A. P.; Chen, J.-H.; Schipper, D. E.; Whitmire, K. H. Thin Films of $(Fe_{1-x}Co_x)_3P$ and $Fe_3(P_{1-x}Te_x)$ from the Co-Decomposition of Organometallic Precursors by MOCVD. *Chem. Mater.* **2016**, *28*, 7066–7071.

(7) Callejas, J. F.; McEnaney, J. M.; Read, C. G.; Crompton, J. C.; Biacchi, A. J.; Popczun, E. J.; Gordon, T. R.; Lewis, N. S.; Schaak, R. E. Electrocatalytic and Photocatalytic Hydrogen Production from Acidic and Neutral-PH Aqueous Solutions Using Iron Phosphide Nanoparticles. *ACS Nano* **2014**, *8*, 11101–11107.

(8) Yan, Y.; Xia, B. Y.; Ge, X.; Liu, Z.; Fisher, A.; Wang, X. A Flexible Electrode Based on Iron Phosphide Nanotubes for Overall Water Splitting. *Chem. – Eur. J.* **2015**, *21*, 18062–18067.

(9) Yan, Y.; Thia, L.; Xia, B. Y.; Ge, X.; Liu, Z.; Fisher, A.; Wang, X. Construction of Efficient 3D Gas Evolution Electrocatalyst for Hydrogen Evolution: Porous FeP Nanowire Arrays on Graphene Sheets. *Adv. Sci.* **2015**, *2*, 1500120.

(10) Lv, C.; Peng, Z.; Zhao, Y.; Huang, Z.; Zhang, C. The Hierarchical Nanowires Array of Iron Phosphide Integrated on a Carbon Fiber Paper as an Effective Electrocatalyst for Hydrogen Generation. *J. Mater. Chem. A* **2016**, *4*, 1454–1460.

(11) Tian, L.; Yan, X.; Chen, X. Electrochemical Activity of Iron Phosphide Nanoparticles in Hydrogen Evolution Reaction. *ACS Catal.* **2016**, *6*, 5441–5448.

(12) Son, C. Y.; Kwak, I. H.; Lim, Y. R.; Park, J. FeP and FeP_2 Nanowires for Efficient Electrocatalytic Hydrogen Evolution Reaction. *Chem. Commun.* **2016**, *52*, 2819–2822.

(13) Zhang, Y.; Zhang, H.; Feng, Y.; Liu, L.; Wang, Y. Unique Fe_2P Nanoparticles Enveloped in Sandwichlike Graphited Carbon Sheets as Excellent Hydrogen Evolution Reaction Catalyst and Lithium-Ion Battery Anode. *ACS Appl. Mater. Interfaces* **2015**, *7*, 26684–26690.

(14) Liu, M.; Yang, L.; Liu, T.; Tang, Y.; Luo, S.; Liu, C.; Zeng, Y. Fe_2P/Reduced Graphene Oxide/Fe_2P Sandwich-Structured Nanowall Arrays: A High-Performance Non-Noble-Metal Electrocatalyst for Hydrogen Evolution. *J. Mater. Chem. A* **2017**, *5*, 8608–8615.

(15) Read, C. G.; Callejas, J. F.; Holder, C. F.; Schaak, R. E. General Strategy for the Synthesis of Transition Metal Phosphide Films for Electrocatalytic Hydrogen and Oxygen Evolution. *ACS Appl. Mater. Interfaces* **2016**, *8*, 12798–12803.

(16) Callejas, J. F.; Read, C. G.; Popczun, E. J.; McEnaney, J. M.; Schaak, R. E. Nanostructured Co_2P Electrocatalyst for the Hydrogen Evolution Reaction and Direct Comparison with Morphologically Equivalent CoP. *Chem. Mater.* **2015**, *27*, 3769–3774.

(17) Tian, L.; Yan, X.; Chen, X.; Liu, L.; Chen, X. One-Pot, Large-Scale, Simple Synthesis of Co_xP Nanocatalysts for Electrochemical Hydrogen Evolution. *J. Mater. Chem. A* **2016**, *4*, 13011–13016.
(18) Tian, L.; Murowchick, J.; Chen, X. Improving the Activity of Co_xP Nanoparticles for the Electrochemical Hydrogen Evolution by Hydrogenation. *Sustain. Energy Fuels* **2017**, *1*, 62–68.
(19) Tian, J.; Liu, Q.; Cheng, N.; Asiri, A. M.; Sun, X. Self-Supported Cu_3P Nanowire Arrays as an Integrated High-Performance Three-Dimensional Cathode for Generating Hydrogen from Water. *Angew. Chem. Int. Ed.* **2014**, *53*, 9577–9581.
(20) Popczun, E. J.; McKone, J. R.; Read, C. G.; Biacchi, A. J.; Wiltrout, A. M.; Lewis, N. S.; Schaak, R. E. Nanostructured Nickel Phosphide as an Electrocatalyst for the Hydrogen Evolution Reaction. *J. Am. Chem. Soc.* **2013**, *135*, 9267–9270.
(21) Kresse, G.; Hafner, J. Ab Initio Molecular Dynamics for Liquid Metals. *Phys. Rev. B* **1993**, *47*, 558–561.
(22) Kresse, G.; Furthmüller, J. Efficiency of Ab-Initio Total Energy Calculations for Metals and Semiconductors Using a Plane-Wave Basis Set. *Comput. Mater. Sci.* **1996**, *6*, 15–50.
(23) Kresse, G.; Furthmüller, J. Efficient Iterative Schemes for *Ab Initio* Total-Energy Calculations Using a Plane-Wave Basis Set. *Phys. Rev. B* **1996**, *54* (16), 11169–11186.
(24) Larsen, A. H.; Mortensen, J. J.; Blomqvist, J.; Jacobsen, K. W. The Atomic Simulation Environment—a Python Library for Working with Atoms. *J. Phys. Condens. Matter* **2017**, *29*, 273002.
(25) Wellendorff, J.; Lundgaard, K. T.; Møgelhøj, A.; Petzold, V.; Landis, D. D.; Nørskov, J. K.; Bligaard, T.; Jacobsen, K. W. Density Functionals for Surface Science: Exchange-Correlation Model Development with Bayesian Error Estimation. *Phys. Rev. B* **2012**, *85*, 235149.
(26) Mortensen, J. J.; Kaasbjerg, K.; Frederiksen, S. L.; Nørskov, J. K.; Sethna, J. P.; Jacobsen, K. W. Bayesian Error Estimation in Density-Functional Theory. *Phys. Rev. Lett.* **2005**, *95*, 216401.
(27) Blöchl, P. E. Projector Augmented-Wave Method. *Phys. Rev. B* **1994**, *50*, 17953–17979.
(28) Monkhorst, H. J.; Pack, J. D. Special Points for Brillouin-Zone Integrations. *Phys. Rev. B* **1976**, *13*, 5188–5192.
(29) Bengtsson, L. Dipole Correction for Surface Supercell Calculations. *Phys. Rev. B* **1999**, *59*, 12301–12304.
(30) Jain, A.; Ong, S. P.; Hautier, G.; Chen, W.; Richards, W. D.; Dacek, S.; Cholia, S.; Gunter, D.; Skinner, D.; Ceder, G.; Persson, K.A. Commentary: The Materials Project: A Materials Genome Approach to Accelerating Materials Innovation. *APL Mater.* **2013**, *1*, 011002.
(31) Docherty, R.; Clydesdale, G.; Roberts, K. J.; Bennema, P. Application of Bravais-Friedel-Donnay-Harker, Attachment Energy and Ising Models to Predicting and Understanding the Morphology of Molecular Crystals. *J. Phys. Appl. Phys.* **1991**, *24*, 89–99.
(32) Kibsgaard, J.; Tsai, C.; Chan, K.; Benck, J. D.; Nørskov, J. K.; Abild-Pedersen, F.; Jaramillo, T. F. Designing an Improved Transition Metal Phosphide Catalyst for Hydrogen Evolution Using Experimental and Theoretical Trends. *Energy Env. Sci* **2015**, *8*, 3022–3029.
(33) Chung, D. Y.; Jun, S. W.; Yoon, G.; Kim, H.; Yoo, J. M.; Lee, K. S.; Kim, T.; Shin, H.; Sinha, A. K.; Kwon, S. G.; Kang, K.; Hyeon, T.; Sung, Y-E. Large-Scale Synthesis of

Carbon-Shell-Coated FeP Nanoparticles for Robust Hydrogen Evolution Reaction Electrocatalyst. *J. Am. Chem. Soc.* **2017**, *139*, 6669–6674.

(34) Santos-Carballal, D.; Roldan, A.; Grau-Crespo, R.; de Leeuw, N. H. A DFT Study of the Structures, Stabilities and Redox Behaviour of the Major Surfaces of Magnetite Fe_3O_4. *Phys Chem Chem Phys* **2014**, *16*, 21082–21097.

(35) Nørskov, J. K.; Bligaard, T.; Logadottir, A.; Kitchin, J. R.; Chen, J. G.; Pandelov, S.; Stimming, U. Trends in the Exchange Current for Hydrogen Evolution. *J. Electrochem. Soc.* **2005**, *152* J23-J26.

(36) Seh, Z. W.; Kibsgaard, J.; Dickens, C. F.; Chorkendorff, I.; Nørskov, J. K.; Jaramillo, T. F. Combining Theory and Experiment in Electrocatalysis: Insights into Materials Design. *Science* **2017**, *355*, eaad4998.